UC Berkeley
UC Berkeley Previously Published Works

Title

T Helper Cell Cytokines Modulate Intestinal Stem Cell Renewal and Differentiation

Permalink

https://escholarship.org/uc/item/3rv9j6tg

Journal

Cell, 175(5)

ISSN

0092-8674

Authors

Biton, Moshe
Haber, Adam L
Rogel, Noga
et al.

Publication Date

2018-11-01

DOI

10.1016/j.cell.2018.10.008

Peer reviewed

T helper cell cytokines modulate intestinal stem cell renewal and differentiation

Moshe Biton[#1,2], Adam L. Haber[#1], Noga Rogel[#1], Grace Burgin[1], Semir Beyaz[3,4,5], Alexandra Schnell[6], Orr Ashenberg[1], Chien wen Su[7], Christopher Smillie[1], Karthik Shekhar[1], Zuojia Chen[6], Chuan Wu[6], Jose Ordovas-Montanes[8,9,10,11], David Alvarez[12], Rebecca H. Herbst[1,13], Mei Zhang[7], Itay Tirosh[1,14], Danielle Dionne[1], Lan T. Nguyen[1], Michael E. Xifaras[3], Alex K. Shalek[8,9,10,11], Ulrich H. von Andrian[12], Daniel B. Graham[9], Orit Rozenblatt-Rosen[1], Hai Ning Shi[7], Vijay Kuchroo[6,9], Omer H. Yilmaz[3,9,15], Aviv Regev[1,3,16,§], and Ramnik J. Xavier[2,9,17,18,19,§]

[1]Klarman Cell Observatory, Broad Institute of Harvard and MIT, Cambridge, MA 02142, USA

[2]Department of Molecular Biology, Massachusetts General Hospital, Boston, MA, 02114, USA

[3]The David H. Koch Institute for Integrative Cancer Research at MIT, Department of Biology, MIT, Cambridge, Massachusetts 02139, USA.

[4]Division of Hematology/Oncology, Boston Children's Hospital and Department of Pediatric Oncology, Dana-Farber Cancer Institute, Howard Hughes Medical Institute, Harvard Stem Cell Institute, Harvard Medical School, Boston, Massachusetts 02115, USA.

[5]Cold Spring Harbor Laboratory, Cold Spring Harbor, NY 11724

[6]Evergrande Center for Immunologic Diseases, Brigham and Women's Hospital, Harvard Medical School, Boston, Massachusetts, USA.

[7]Mucosal Immunology and Biology Research Center, Massachusetts General Hospital and Harvard Medical School, Charlestown, MA, 02129, USA.

[8]Institute for Medical Engineering & Science (IMES) and Department of Chemistry, Massachusetts Institute of Technology (MIT), Cambridge, MA 02139, USA.

[9]Broad Institute of Harvard and MIT, Cambridge, MA 02142, USA

[10]Ragon Institute of MGH, MIT, and Harvard, Cambridge, MA 02139, USA

[11]The David H. Koch Institute for Integrative Cancer Research at MIT, Cambridge, MA 02142

[12]Department of Microbiology & Immunobiology and Center for Immune Imaging, Harvard Medical School, Boston, MA 02115, USA.

[13]Department of Systems Biology, Harvard Medical School, Boston, MA 02114, USA

[14]Department of Molecular Cell Biology, Weizmann Institute of Science, Rehovot 7610001, Israel.

[15]Department of Pathology, Massachusetts General Hospital, Boston, MA 02114, USA.

[16]Howard Hughes Medical Institute, Department of Biology, Massachusetts Institute of Technology, Cambridge, MA 02140, USA

[17]Gastrointestinal Unit and Center for the Study of Inflammatory Bowel Disease, Massachusetts General Hospital, Boston, MA, 02114, USA

[18]Center for Microbiome informatics and Therapeutics, MIT

[19]Lead contact

[#] These authors contributed equally to this work.

Summary

In the small intestine, a niche of accessory cell types supports the generation of mature epithelial cell types from intestinal stem cells (ISCs). It is unclear however if and how immune cells in the niche affect ISC fate or the balance between self-renewal and differentiation. Here, we use single-cell RNA-seq to identify MHC class II (MHCII) machinery enrichment in two subsets of Lgr5^{+} ISCs. We show that MHCII^{+} Lgr5^{+} ISCs are non-conventional antigen presenting cells in co-cultures with CD4^{+} T helper (Th) cells. Stimulation of intestinal organoids with key Th cytokines affects Lgr5^{+} ISC renewal and differentiation in opposing ways: pro-inflammatory signals promote differentiation, while regulatory cells and cytokines reduce it. *In vivo* genetic perturbation of Th cells or MHCII expression on Lgr5^{+} ISCs impacts epithelial cell differentiation and IEC fate during infection. These interactions between Th cells and Lgr5^{+} ISCs thus orchestrate tissue-wide responses to external signals.

In brief

Intestinal stem cells act as non-conventional antigen presenting cells and these interactions with T helper cells modulate ISC renewal and differentiation to shape the intestine

---

INTRODUCTION

To maintain tissue homeostasis the gut epithelium constantly regenerates by rapid proliferation and differentiation (van der Flier and Clevers, 2009), from intestinal stem cells (ISCs), to committed progenitors, to specific intestinal epithelial cell (IEC) types (Barker et al., 2007; van der Flier and Clevers, 2009). ISC differentiation depends on external signals, from both epithelial and non-epithelial cells, especially stromal cells (Degirmenci et al., 2018; Shoshkes-Carmel et al., 2018).

Several studies have shown important roles for immune cells in tissue homeostasis. Tissue-resident innate immune cells can play a role in regeneration of the gut (Lindemans et al., 2015; Saha et al., 2016) and other tissues (Aurora and Olson, 2014; Stappenbeck and Miyoshi, 2009). Among adaptive immune cells, recent studies have implicated T regulatory cells (T_{regs}) in tissue regeneration processes in the muscles and lungs (Arpaia et al., 2015; Burzyn et al., 2013), and T cytotoxic cells were shown to eliminate Lgr5^{+} ISCs via MHC class I (Agudo et al., 2018). Skin-resident T_{regs} were recently shown to help maintain hair follicle stem cell (HFSC) renewal via Notch signaling (Ah et al., 2017), but a similar role in the gut has not been reported.

Here, using single cell RNA-seq (scRNA-seq), we found Lgr5^{+} ISC subsets with enriched expression of MHC class II (MHCII) molecules. We showed that Lgr5^{+} ISCs stimulated with antigen can present to and interact with Th cells. We characterized the functional impact of ISC-T cell interactions in organoid assays and in mouse models during homeostasis or infections, finding opposing effects of key inflammatory and regulatory Th cells and cytokines on Lgr5^{+} ISC renewal and differentiation, and highlighting a new functional axis for gut homeostasis.

RESULTS

High expression of MHCII genes by ISC subsets

To search for a ISC-immune cell interaction, we queried our recent scRNA-seq data of 1,522 EpCAM[+] intestinal epithelial cells (IECs) (Haber et al., 2017) from WT and Lgr5-GFP mice (Barker et al., 2007) for genes expressed by ISCs that encode cell surface or secreted proteins known to interact with immune cells. ISCs partitioned into three sets (ISC-I, II, III, Figure 1A,B), all expressing known stem cells markers, including *Lgr5* (Figure 1D, S1A,B, Table S1), consistent with recent reports (Yan et al., 2017). By expression signatures, flow cytometry, and immunofluorescence assays (IFA), we identified an ISC subset that is low-cycling (ISC-I), and two more proliferative ISC subsets (ISC-II and III, Figure S1C-E). All subsets are present in similar proportions in the duodenum, jejunum, and ileum (Figure S1F, STAR Methods). Pseudotime analysis (Haghverdi et al., 2015) suggested that ISC-I have the most stem-like features, while ISC-II and ISC-III are progressively more differentiated (Figure 1C and S1H,I), although these may not reflect a developmental order as IECs can de-differentiate (Buczacki et al., 2013; Tetteh et al., 2016).

Querying annotated receptor genes (Ramilowski et al., 2015) that are differentially expressed (DE) between ISCs and the other IECs (Figure S1G and Table S2) identified *Cd74,* which encodes the invariant chain of the MHCII complex, as enriched in ISCs (Figure 1E,F, S1G and S2A). This expression was enriched in ISC-II and ISC-III, which also co-expressed many other canonical components of the MHCII machinery and the non-canonical co-stimulatory molecules *Sectm1a* and *Sectm1b* (Howie et al., 2013; Wang et al., 2012) (Figure 1F). MHCII expression has been previously described in IECs (Bland and Warren, 1986; Thelemann et al., 2014), but its ISC enrichment was not reported. We validated enriched MHCII protein expression by Lgr5^{+} ISCs by FACS and *in situ* in wild type mice, and its absence in a constitutive MHCII knockout (KO) (Madsen et al., 1999) (Figure 1G

and S2B,C). We further showed that MHCII[+]Lgr5^{+} ISCs (ISC-II and -III) are more proliferative then ISC-I (Figure S2D,E).

MHCII[+] Lgr5^{+} ISCs functionally present antigen to Th cells

IECs have been previously shown to present class II antigens and interact with Th cells (Bland and Warren, 1986; Kaiserlian et al., 1989). We hypothesized that among IECs, it is Lgr5^{+} ISCs that interact with Th cells via MHCII. Intravital imaging showed that Th cells are in close proximity to Lgr5^{+} ISCs in small intestinal crypts (Figure S3B, red arrows and movie S1).

To test this hypothesis, we sorted EpCAM^{+} cells, which contains Lgr5^{+} ISCs (Figure S1B), and cultured them with DQ-ovalbumin (DQ-Ova), a self-quenching conjugate of ovalbumin that fluoresces upon proteolytic degradation. (We could not use Lgr5-GFP^{+} cells, as the fluorescence of GFP and quenched DQ-Ova may overlap.) Approximately 10% of EpCAM^{+} cells had high fluorescence, compared to ~40% of dendritic cells (DCs) (Figure 2A). A stem cell signature was highly enriched in DQ-Ova[+] EpCAM^{+} cells compared to all EpCAM^{+} cells by scRNA-seq (Figure 2B). Thus, ISCs within EpCAM^{+} cells largely account for their ability to process extracellular antigens.

Next, we showed that Lgr5^{+} ISCs activate Th cells *in vitro* in an antigen-specific manner. We enriched for EpCAM[+]-Lgr5-GFP[high] ISCs, EpCAM[+]GFP[−] IECs (which include non-GFP Lgr5^{+} ISCs due to the mosaic nature of this mouse model), or DCs from the lamina propria (LP) of Lgr5-GFP mice (n=9 mice). We co-cultured each subset in the presence of ovalbumin (Ova) peptide with naïve OTII Th cells that specifically recognize Ova peptide 323-339-MHCII complexes (OTII, STAR Methods). OTII cells co-cultured with EpCAM[+]GFP^{−} cells led to a modest increase in IL-2 protein secretion as previously reported (Bland and Warren, 1986; Kaiserlian et al., 1989) (Figure 2C). Compared to EpCAM[+]GFP^{−} cells, co-culture with Lgr5-GFP[+] ISCs or DCs caused substantially higher OTII activation by IL-2 secretion (~3- and 21-fold higher, Figure 2C), and T cell proliferation (65.8% and 89.5% vs. 32.6%, Figure S3 A). These results indicate that *in vitro* Lgr5^{+} ISCs interact and activate naive Th cells via MHCII presentation of peptides.

Th cytokines regulate Lgr5^{+} ISC renewal and differentiation

To investigate the impact of the Th-ISCs interaction on ISCs, we next used an intestinal organoid culture in which immune cells are absent but can be added in a controlled manner (Figure S3D). We isolated the effect of MHCII by using prolonged cultured organoids (2 weeks) (Sato et al., 2009), in which Lgr5^{+} ISCs lose expression of MHCII (Figure S3C). We added to the organoid cultures either polarized, cytokine-producing, Th cell subsets (Th1, Th2, Th17, or inducible T_{reg} (iT_{reg}) cells) (Jager et al., 2009) or their respective key cytokines (interferon gamma (IFNγ), interleukin 13 (IL-13), IL-17A, or IL-10). We also tested IL-22, as it shares the same receptor subunit with IL-10. IECs, including ISCs, expressed receptors for Th cytokines IFNγ, IL-13, IL-4, IL-17A, IL-10 (IL-10rb), and IL-22 (Figure S1J), although IL-10ra expression was detectable only in bulk quantitative PCR at low levels (data not shown), as previously reported (Denning et al., 2000). We collected scRNA-seq profiles for each condition. For the Th co-cultures, we computationally

distinguished (*post-hoc*) epithelial cells from T cells by their profiles. We confirmed by FACS that each Th subset expressed key cytokines and TFs prior to co-culture (data not shown); and by scRNA-seq that they maintain this expression during co-culture (Figure S3E). However, *ex vivo* polarized Th cells did not fully recapitulate their *in vivo* counterparts: Th2 differentiation yielded less than 20% IL-4 and IL-13 expressing cells, while other Th subsets had higher differentiation rates (data not shown). There are also differences between organoids and IECs: goblet and Paneth lineages do not fully diverge (Figure S3F), as we also observed in another organoid scRNA-seq dataset (Grün et al., 2015) (data not shown).

Both co-culture with iT_{regs} and stimulation with IL-10 led to ISC expansion within organoids, while co-cultures with Th1, Th2 and Th17 cells or treatment with IL-13 or IL-17 all decreased the ISC pool based on clustering (Figure 2D,E, S3G-I and Table S3). This effect was highlighted along the stem cell differentiation continuum by diffusion maps (Haghverdi et al., 2015): cells from IL-10-treated organoids had a significantly more "stem-like" pseudotime distribution, while cells from IL-13 treated organoids showed the opposite effect (Figure 2F). IL-22 treatment increased enterocyte numbers and organoid growth (data not shown), as shown previously (Lindemans et al., 2015) and distinct from IL-10's effect.

Consistent with their depleted stem cell pool, organoids co-cultured with Th1, Th2, or Th17 cells or treated with IL-17a had expanded numbers of transit amplifying (TA) cells (Figure 2D,E). MHCII was elevated in IECs in Th1 co-cultures (Figure S3C). However, at the low concentration of IFNγ (0.5μ/ml) we used to avoid organoid apoptosis (Farin et al., 2014), we did not observe the expected up-regulation of MHCII genes. IL-13 treatment decreased the proportion of secretory 'Paneth-goblet' cells, and increased tuft cells, as previously described (Gerbe et al., 2016; Howitt et al., 2016; von Moltke et al., 2016) (Figure 2D,F and S3J,K); and Th1 co-culture up-regulated Paneth cell-specific genes (Figure 2E and S3K,L).

The effects of Th cytokines on the ISC pool suggest that they modulate ISC renewal potential (Figure 2D-F), which in turn should affect the ability of ISCs to form organoid cultures. To test this, we measured how many organoids grew three days after re-seeding of equal numbers of cytokine-treated organoids (*n*=6 per group, STAR Methods) (Beyaz et al., 2016). We observed a significant reduction in the clonogenicity of organoids treated with IL-13, whereas IL-10 induced higher clonogenicity (Figure 2G), confirming that Th cytokines impact ISC renewal.

The ISC pool expands when MHCII is genetically ablated in epithelial cells *in vivo*

To assess the role of MHCII in IECs under homeostatic conditions *in vivo* we next examined a MHCII conditional KO model. We crossed H2-Ab1^{fl/fl} mice (Hashimoto et al., 2002) to Villin-Cre-ER[T2] mice (el Marjou et al., 2004), generating a mouse model of specific and inducible MHCII KO in IECs (MHCII [gut], STAR Methods). We profiled 1,559 MHCII [gut] IECs and 1,617 MHCII^{fl/fl} IECs (*n*=5 mice per group) 10 days post-tamoxifen (Tam) induction. We validated MHCII ablation in IECs (Figure 3A and S4A), but not in DCs of the mesenteric lymph node and LP (Figure S4B and data not shown).

Clustering revealed a 17.6% increase in ISCs proportion in MHCII ^{gut} mice (Figure 3C and S4D,E). Moreover, there was a 30.3% increase in *Lgr5*-expressing cells in MHCII ^{gut} mice by scRNA-seq (Figure S4C), which we confirmed with *Lgr5* and *Olfm4 in situ* (Figure 3B and data not shown). Consistently, ISC markers were overrepresented among the genes up-regulated in cells from MHCII ^{gut} mice (Figure S4F). Within all ISCs from MHCII ^{gut} mice, the proportion of ISC-II cells was significantly higher, while that of ISC-III cells was significantly lower (Figure 3D). Importantly, there was a reduction in CD4$^+$ cells in the crypt LP of MHCII ^{gut} mice (Figure 3E), while the number of CD4$^+$ cells in the villus LP was unchanged (Figure S4G).

We also confirmed this effect in Lgr5$^+$ ISC-specific inducible MHCII KO mice (MHCII ^{ISC}, STAR Methods) generated by crossing Lgr5-GFP mice with H2-Ab1$^{fl/fl}$ mice. Ten days post-Tam treatment resulted in ablation of MHCII in Lgr5 GFP$^+$ ISCs and their progeny tested by IFA (Figure 3F) and flow cytometry, while CD11c$^+$ cells from the LP retained MHCII expression (data not shown). Lgr5$^+$ ISCs were expanded in MHCII ^{ISC} mice based on FACS and IFA of Lgr5 GFP$^+$ ISCs (Figure 3G,H and S4H, *n*=5 mice). Co-culture with Lgr5$^+$ ISCs from MHCII ^{ISC} did not activate naïve OTII cells in the presence of Ova peptide, in contrast to robust activation by MHCII-proficient Lgr5$^+$ ISCs (Figure 3I **and** S3A). These results indicate that ablation of MHCII in IECs in general (MHCII ^{gut}) or in Lgr5$^+$ ISCs specifically (MHCII ^{ISC}) eliminated the ability of ISCs to activate T cells in co-culture, and increased Lgr5$^+$ ISC numbers and the expression of ISCs markers.

MHCII$^+$ Lgr5$^+$ ISCs are involved in IEC remodeling during infection

To examine IEC remodeling *in vivo*, we next analyzed scRNA-seq data of 9,842 IECs (Haber et al., 2017) and 5,122 CD45$^+$ immune cells (STAR Methods) from mice infected with *Salmonella enterica* (*Salmonella*) or *Heligmosomoides polygyrus* (*H. polygyrus*) (Haber et al., 2017). As expected, *Salmonella* induced Th1 responses (Figure S5A-C; Table S4) and an increase in Paneth cell numbers, while *H. polygyrus* caused tuft cell expansion (Haber et al., 2017) (Figure S5D,E). There was a mild reduction in the expression of a pan-stem signature (Figure 4A and S5F), but a substantial increase in MHCII expression (Figure 4B **and** S5F) and a shift in the relative proportions of the three ISC subsets (Figure 4C and S5G), with reduction in cells expressing the ISC-I program and elevation of those expressing the ISC-II and -III programs (Figure 4C,D).

We next assessed the role of MHCII in ISC differentiation by concurrently infecting mice with *H. polygyrus* for 3 days and treating them with either MHCII-blocking (α-MHCII) or control anti-IgG (α-IgG) antibodies, followed by scRNA-seq and cell-type identification (Figure 4E). Compared to α-IgG treated control, mice treated with α-MHCII showed reduced tuft cell proportions post-infection and increased ISC proportions (Figure 4E,F). This experiment, however, cannot exclude indirect effects of α-MHCII, such as impacting APCs directly, which in turn affect Th2 differentiation (Ziegler and Artis, 2010).

We therefore tested the impact of MHCII deletion in IECs during *H. polygyrus* infection, using either a constitutive epithelial H2-Ab1 KO driven by the Villin promoter (Madison et al., 2002) (MHCII$^{gut-/-}$, STAR Methods), or the MHCII ^{ISC} model. For MHCII ^{ISC}, to minimize indirect effects, we induced the conditional KO shortly before infection (6 days).

There was little or no tuft cell expansion in both mouse models four days (MHCII[gut−/−]) or 10 days (MHCII [ISC]) post-infection, in marked contrast to the expansion in infected matched controls (Figure 5A-C). Conversely, *Lgr5* expression was up-regulated in MHCII [ISC] mice during infection compared to MHCII^{fl/fl} controls (Figure 5C). Importantly, MHCII[gut−/−] mice infected with 200 *H. polygyrus* larvae had higher worm burden compared to MHCII^{fl/fl} controls after 6 weeks of infection (66 ±12.46 *vs.* 16.17±5.94 worms/mouse (mean ± SD); n=6 mice/group; p<0.005, t-test).

MHCII deletion in the epithelial compartment activates the local immune system

The immune compartment – especially DCs and Th cells – was substantially modulated in both homeostasis and *H. polygyrus* infection after MHCII ablation in IECs (Figure 5D-J). We performed scRNA-Seq of CD45^{+} cells from the LP of MHC[gut−/−] and MHCII^{fl/fl} mice, at homeostasis and 4 days post-infection (n=3 in each group, 24,649 cells overall, Figure 5E), and tested immune cell markers *in situ.* (Due to the mosaic nature of MHCII [ISC], we did not profile their immune cells.) First, during infection, only macrophage and DC proportions were significantly affected by IEC-MHCII deletion (Figure 5F,G), with a particularly strong increase (61.6%) in DCs in MHCII[gut−/−] post-infection (but not at baseline). Second, although overall Th cell proportions were not affected by the KO in either infection or homeostasis (Figure 5F), Th cells from uninfected MHCII[gut−/−] mice expressed higher levels of a T cell activation signature compared to controls (Figure 5H,I, Table S5, STAR Methods). This signature was further increased to comparable levels in both MHCII^{fl/fl} and MHCII[gut−/−] mice upon infection (Figure 5I,J). Finally, there was a strong reduction in the number of CD4^{+} cells found in close proximity to Lgr5^{+} ISCs in MHCII[gut−/−] mice following *H. polygyrus* infection by IFA, a reduction also observed in uninfected MHCII [gut] mice (Figure 3E and S4G). Conversely, villus CD4^{+} cell numbers were not affected by the KO (Figure 5D and data not shown). These results suggest that MHCII expression by epithelial cells impacts both the innate and adaptive responses; some of which may propagate indirect effects, for example dendritic cells during infection.

The ISC pool increases in T cell depleted mice

To examine the role of T cells in Lgr5^{+} ISC differentiation axis, we next assessed two T cell-deficient mouse models. We profiled 2,967 IECs from athymic B6 nude mice (Cordier and Haumont, 1980) (*n*=2), characterized by T cell depletion. Clustering revealed significantly higher fractions of ISCs (52.5% increase, STAR Methods), TA, and enteroendocrine cells compared to control mice (*n*=6, Figure S6A,B), and a decrease in enterocyte progenitors. Consistently, ISC markers were enriched (56 of 1,804 genes, Figure S6A and Table S6) among genes overall up-regulated in cells of nude *vs.* controls. Similar analysis of 9,488 IEC profiles from TCRβ KO mice (*n*=2) (Mombaerts et al., 1992), which lack α/β T cells, also showed a significant expansion of the ISC pool (35.0% increase, Figure S6C,D) and a decrease in enterocyte progenitors (as well as an increase in goblet cells). We confirmed the increased expression of *Lgr5* mRNA *in situ* (Figure S6E). Thus, T cell (or only α/β T cells) ablation leads to ISCs accumulation, possibly due to diminished differentiation capacity, in particular toward the absorptive lineage.

T_{regs} help maintain the Lgr5⁺ ISC niche *in vivo*

In our organoid assays, only T$_{reg}$ cells and their key cytokine IL-10 promoted renewal of the ISC pool. To confirm this *in vivo*, we used *Foxp3*-DTR mice (Kim et al., 2007), in which T$_{regs}$ are depleted upon administration of diphtheria toxin (DT). Foxp3$^+$ T$_{regs}$ are the major source of *Il10* expression based on our LP scRNA-seq (data not shown). To minimize indirect effects, we induced T$_{reg}$ depletion with DT for only 4 or 7 days (Chinen et al., 2010; Kim et al., 2007). We confirmed T$_{reg}$ ablation in the LP (Figure S7A), and observed higher proliferation rates, including of ISCs, and no signs of increased cell death or major gut inflammation in intestinal crypts of *Foxp3*-DTR *vs.* control mice (Figure S7B,C). However, Th cell numbers in both the mesenteric lymph nodes and LP were elevated after DT induction (Figure S7D,E), and in particular at intestinal crypts in close proximity to Lgr5$^+$ ISCs (Figure 6A and S7E). Overall, this shows that T$_{reg}$ ablation for 4 and 7 days precedes apparent tissue damage. Next, we profiled 3,387 IECs from day 7 *Foxp3*-DTR (*n*=4) and matched control (*n*=5) mice treated with DT. Consistent with our hypothesis, IEC differentiation was aberrant, with a substantial increase in enterocyte progenitors, tuft and goblet cells, and reduction in mature enterocytes, by both scRNA-seq and IFA (Figure 6B and S7F,G).

Importantly, Lgr5$^+$ ISC proportions were significantly reduced by several measures: (**1**) Clustering of scRNA-seq from day 7 (66.3% decrease, Figure 6C and S7F); (**2**) *Lgr5 in situ* stain (Figure 6D); (**3**) Fraction of Lgr5$^+$ cells in scRNA-Seq data (Figure S7H); and (**4**) Over-representation of ISC genes among those down-regulated in T$_{reg}$-depleted mice (Figure S7I). In addition, ISCs showed elevated MHCII expression (Figure 6E,F) and increased proliferation by Ki67 staining and expression of a cell cycle signature (Figure 6D,F and S7B) and an elevated proportion of MHCII$^+$, proliferative ISC-II and IIIs compared to reduction in the low-cycling MHCIT ISC-I (Figure 6F,G). The reduction in ISCs and a shift towards more MHCII$^+$ proliferative ISCs in Foxp3-DTR mice supports a model of higher differentiation rates and stem cell pool depletion.

DISCUSSION

Previous studies of stem cell dynamics and differentiation focused on epithelial and stromal signals (Sato et al., 2011; Stappenbeck and Miyoshi, 2009). Here, we used scRNA-seq to uncover interactions between Lgr5$^+$ ISCs and the Th cells and their effect on IEC remodeling.

Our results support a model of crosstalk between Th cells and Lgr5$^+$ ISCs in which Th cells or their key cytokines interact with Lgr5$^+$ ISCs and subsequently impact the ISC pool and modulate its differentiation (Figure 7). In this model, T$_{regs}$ and their key cytokine IL-10 help maintain the Lgr5$^+$ ISC niche in the small intestine. T$_{regs}$ ablation resulted in aberrant epithelial cell differentiation: reduction in the Lgr5$^+$ ISC pool and accumulation of differentiated cells. This effect might be enhanced by the concomitant increased accumulation of other Th cells (Th1, Th2 and Th17) in the stem cell niche of T$_{reg}$ ablated mice, which promote Lgr5$^+$ ISC differentiation. Indeed, the Lgr5$^+$ ISC pool is expanded in pan-T or α/β T cells depleted mice.

This model can help explain how the ISC pool is maintained during homeostasis and modulated during infection. Upon bacterial or parasite infection, respectively, both Th1 and Th2 cells and their signature cytokines bias stem cells toward differentiation (at the expense of self-renewal), but with specific IEC-type effects, either increasing Paneth (Th1) or tuft (Th2) cells based on the respective functional demand (*e.g.*, "sweep and weep" for helminth infection (Anthony et al., 2007)). Meanwhile, Th17 cells, reduce the number of Lgr5$^+$ ISCs, which may reflect an overall shift towards stem cell differentiation. As T$_{regs}$ are elevated after a strong inflammatory response (Tanoue et al., 2016), they may serve as negative feedback on differentiation to replenish ISC numbers. Additional mouse models, where specific cytokines or immune cells are conditionally depleted, would help elucidate further connections in this ISC-Th cell circuit.

What is the role of the MHCII system in Lgr5$^+$ ISCs? First, MHCII$^+$ Lgr5$^+$ ISC subsets may act as non-conventional APCs and play a role in activating gut-resident Th cells, although further characterization is needed to determine presentation *in vivo.* Microfold (M) cells are the key sentinels of antigen sampling in the small intestine (Mabbott et al., 2013), but are rare and localized to Peyer's patches. Lgr5$^+$ ISC-mediated presentation could provide an alternate mechanism by which IECs can sense and initiate a response to signals coming from the lumen. Second, the epithelial MHCII machinery is important to maintain appropriate IEC differentiation, possibly by presentation to and contact with Th cells. Third, the MHCII system may be induced by infections. We observed a shift towards MHCII$^+$ Lgr5$^+$ ISC states in both bacterial and helminth infection and showed that during *H. polygyrus* infection, MHCII deletion in IECs or Lgr5$^+$ ISCs inhibits IEC remodeling, elevates Lgr5$^+$ ISC numbers and enhanced infection severity. Thus, ISC-Th interactions via MHCII together with IL-25 mediated tuft-ILC interactions (Howitt et al., 2016; von Moltke et al., 2016) could regulate appropriate host responses against parasites. Moreover, the expression of MHCII genes in IECs is induced by Th1 cells (potent producers of IFNγ) in our organoid co-culture system. Thus, IFNγ-producing cells may play a key role in initiating Th cell-Lgr5$^+$ ISC crosstalk. Finally, MHCII expression in IECs may impact the mucosal immune system. Indeed, because deletion of MHCII led to changes in both DC numbers and Th cells activity, some of the observed phenotypes may be indirectly mediated through additional compartments, such as changes in dendritic cells or ISC states (Nusse et al., 2018) and further work, including lineage tracing of ISC subsets, is still needed to clarify the role of epithelial MHCII.

Taken together, the ISC-Th axis may provide a way to integrate epithelial and immune responses to titrate responses to luminal flora, and avoid continuous inflammation after infection. Lgr5$^+$ ISCs respond to pro- and anti-inflammatory signals to balance between renewal and differentiation, which may boost the desired immune response concordantly with signals arriving from the lumen. It is possible that MHCII expression on stem cells plays a similar role in crosstalk with Th cells in other mucosal or non-mucosal tissues, as a general mechanism by which adaptive immune cells regulate parenchymal stem cells to maintain or restore tissue homeostasis.

STAR Methods

CONTACT FOR REAGENT AND RESOURCE SHARING

Further information and requests for resources and reagents should be directed to and will be fulfilled by the Lead Contacts RJX (xavier@molbio.mgh.harvard.edu).

EXPERIMENTAL MODEL AND SUBJECT DETAILS

Mice—All mouse work was performed in accordance with the Institutional Animal Care and Use Committees (IACUC) and relevant guidelines at the Broad Institute and MIT, with protocols 0055-05-15 and 0612-058-15, respectively. C57BL/6J wild-type, Lgr5-EGFP-IRES-CreER^{T2} (Lgr5-GFP), MHCII-KO, Foxp3-DTR, B6 Nude, TCRβ-KO mice, and B6.Cg-Tg(TcraTcrb)425Cbn/J (OTII) were obtained from the Jackson Laboratory (Bar Harbor, ME). MHCII$^{gut-/-}$, MHCII ^{gut} and MHCII ^{ISC} mice were generated by crossing H2-Ab1$^{fl/fl}$ (Jackson laboratory) with Villin-Cre, Villin-CreER[12] or Lgr5-EGFP-IRES-CreER^{T2}, respectively. Both male and female age-matched mice from 7 to 14 weeks of age were used for all experiments in this study. Littermates of the same genotype, sex and age were randomly assigned to experimental groups. All mice were housed under specific-pathogen-free (SPF) conditions at the Broad Institute or MIT animal facilities; infection experiments were conducted at the laboratory of Dr. HN Shi, maintained under specific pathogen-free conditions at Massachusetts General Hospital (Charlestown, MA), with protocol 2003N000158.

Infection models—*S. enterica* infection, mice were infected with a naturally streptomycin-resistant SL1344 strain of *S. Typhimurium* (10^8 cells).

H. polygyrus was propagated as previously described (Shi et al., 1997). Third-stage larvae (L3) of *H. polygyrus* were obtained by culturing the feces of infected stock CO1 mice on moist filter paper for seven days. Mice were intubated with 200L, in 20/LI of deionized water. The accuracy of the dose was estimated by direct counts of the numbers of larvae in five sham doses, which were dispensed into plastic petri dishes before the experimental infection. At necropsy, the intestine was open longitudinally, and worms were removed for quantification under a binocular microscope (counting only worm tails).

***In vitro* and *ex vivo* cultures**—Naïve OTII cells, were isolated from the spleen of 7-10 weeks old OTII female mice

Th cell polarization *in vitro.* CD4$^+$ naïve (CD44^{low}CD62L$^+$CD25$^-$) T cells were isolated from spleen and lymph nodes of 7–10 weeks old C57BL/6J mice using flow cytometry cell sorting. The purity of isolated T cell populations routinely exceeded 98%. Naïve T cells were stimulated with plate-bound anti-CD3 (145-2C11, 1mg/ml) and anti-CD28 (PV-1, 1mg/ml) and polarizing cytokines (Th1: 4 ng/ml IL-12; Th2: 4 ng/ml IL-4; Th17: 10 ng/ml IL-6, 2 ng/ml TGF-β1; iT$_{reg}$: 5 ng/ml TGF-β1; all cytokines from R&D) (Jager et al., 2009).

METHOD DETAILS

BrdU and EDU incorporation.—EdU or BrdU was injected intraperitoneally (IP) into Lgr5-GFP mice at 100 mg kg^{-1} for 2 or 4 hours before tissue collection.

MHCII deletion in intestinal cells.—Cre activity was induced in 7-10 weeks old H2-Ab1 floxed mice that express or not expressing Cre by intraperitoneal injection (IP) of tamoxifen (Sigma-Aldrich), diluted in corn oil, 4 mg per injection, 3 or 5 times, every other day. Mice were sacrificed 10 or 15 days after the first injection. For *H. polygyrus* infection following MHCII ablation, we induced deletion of MHCII ^{ISC} by 3 injections every other day for 6 days in total prior to infection.

***S. enterica* and *H. polvevrus* infection.—**C57BL/6J, MHCII$^{gut-/-}$ or MHCII ^{ISC} and their control littermates (MHCII$^{fl/fl}$) mice were infected with 200 third-stage larvae of *H. polygyrus*. MHCII ^{ISC} and their control siblings (MHCII$^{fl/fl}$) were induced with 4 mg/injection of Tamoxifen for 6 days prior to *H. polygyrus* infection. Mice were sacrificed 3, 4, 10 days or 6 weeks following *H. polygyrus* infection. For the MHCII blocking experiment, C57BL/6J mice infected with *H. polygyrus* were injected with 500μg of blocking anti-mouse MHCII antibody (BioXCell) or Rat IgG2b isotype control (BioXCell) one-day prior to and for 2 consecutive days after *H. polygyrus* infection. For *S. enterica* infection, C57BL/6J mice were infected with a naturally streptomycin-resistant SL1344 strain of *S. Typhimurium* (10^8 cells) and were sacrificed 48 hours after infection.

Diphtheria toxin.—Foxp3-DTR and wild-type C57BL/6J mice were injected intraperitoneally with diphtheria toxin (DT) at 22.5ng/g body weight every other day for either 4 or 7 days and then sacrificed for tissue collection.

Epithelial cell dissociation and crypt isolation.—For all mice, crypts were isolated from the whole small intestine or the duodenum, jejunum and ileum compartments to account for regional distribution of Lgr5$^+$ ISCs. The small intestine was extracted and rinsed in cold PBS. The tissue was opened longitudinally and sliced into small fragments roughly 0.2 cm long. The tissue was incubated in 20mM EDTA-PBS on ice for 90 min, while shaking every 30 min. The tissue was then shaken vigorously and the supernatant was collected as fraction 1 in a new conical tube. The tissue was incubated in fresh EDTA-PBS and a new fraction was collected every 30 min. Fractions were collected until the supernatant consisted almost entirely of crypts. The final fraction (enriched for crypts) was filtered through a 70μm filter, washed twice in PBS, centrifuged at 300g for 3 min, and dissociated with TrypLE Express (Invitrogen) for 1 min at 37°C. The single-cell suspension was then passed through a 40μm filter and stained for fluorescence- activated cell sorting (FACS) machine (Astrios) sorting for either scRNA-seq method (below).

Immune cell isolation.—Immune cells from the Lamina Propria were isolated enzymatically by incubating the small intestine with Liberase TM (100 μg/mL, Sigma) and DNasel (10 μg/mL, Sigma) for 30 min at 37°C. Immune cells were also isolated from the mesenteric lymph nodes (mLN). Cells were then incubated with CD3, CD4, CD45, TCRβ,

CD11c, I-A/I-E, IL17a, IFNγ or IL13 FACS-labeled antibodies and either used for analysis or sorted for scRNA-seq.

Naïve OTII cells were isolated from the spleen of 7-10 week old OTII mice. Cells were purified using the Naïve CD4+ T Cell Isolation Kit (Miltenyi Biotec, 130-104-453) per manufacturer's recommendations. Cells were then FACS sorted for CD25$^-$CD4$^+$CD44^{low}CD62L$^+$ to obtain 99% purity of naïve OTII cells.

Intestinal organoid cultures—Following crypt isolation from the whole small intestine of both male and female mice, the single-cell suspension was re-suspended in Matrigel (BD Bioscience) with 1µM Jagged-1 peptide (Ana-Spec). Roughly 300 crypts embedded in 25µl of Matrigel were seeded onto each well of a 24-well plate. Once solidified, the Matrigel was incubated in 600µl culture medium (Advanced DMEM/F12, Invitrogen) with streptomycin/penicillin and glutamatax and supplemented with EGF (100 ng/mL, Peprotech), R-Spondin-1 (600ng/mL, R&D), Noggin (100ng/mL, Prepotech), Y-276432 dihydrochloride monohydrate (10µM, Tochris), N-acetyl-1-cysteine (1µM, Sigma-Aldrich), N2 (1X, Life Technologies), B27 (IX, Life Technologies) and Wnt3A (25ng/mL, R&D Systems). Fresh media was replaced on day 3, and organoids were passaged by dissociation with TrypLE and re-suspended in new Matrigel on day 6 with a 1:3 split ratio.

T helper cell co-culture experiments.: Organoids were cultured with Th1, Th2, Th17 or iT$_{regs}$. Roughly 10,000 T helper cells were added to each well of 500 organoids and were supplemented either to the medium or suspended in the Matrigel. Treated organoids were dissociated and subjected to droplet based scRNA-seq.

Cytokine treated organoids.: Organoids were additionally treated with 0.5u/ml IFNγ, 20 ng/ml IL-13, 20 ng/ml IL-17A or 10ng/ml IL-10 in the culture medium for 3 days.

Re-seeding after cytokine treatment.: 500 organoids/well were treated with cytokines, as in the cytokine treated organoids above, collected after 3 days and then re-seeded at 500 organoids/well in fresh media without cytokines. Each day, images were taken at 2X magnification and quantification of organoids number was performed with the ImageJ software.

Antigen processing and presentation—*Processing.* 3×10^4 sort-purified CD11c$^+$ DCs from the spleen or EpCAM$^+$ cells isolated from the small intestine were cultured with 10µg/ml DQ Ovalbumin (Thermo Fisher Scientific) at 4°C, 37°C or with no DQ Ovalbumin for two hours, washed and analyzed via flow cytometry. Additionally, EpCAM$^+$ DQ$^+$ cells were FACS sorted individually into 96 well plates with TCL and 1% 2-mercaptoethanol and then processed via plate-based scRNA-seq (as described below).

Presentation.: 5×10^3 sort-purified Lgr5^{high} EpCAM$^+$, 5×10^3 sort-purified Lgr5^{negative} EpCAM$^+$ or 2.5×10^3 CD11c$^+$ DCs were cultured with 5×10^4 naïve OTII cells in the organoid culture medium above (without Matrigel), with or without 15µg/ml Ovalbumin peptide (Anaspec, OVA323-339) at 37°C for 72 hours. T cell activation was measured through IL-2 levels in the supernatant using the BD Cytometric Bead Array Mouse IL-2

Flex Set (BD Bioscience) per manufacturer's directions. Capture bead solution was added to the supernatant, followed by the detection bead solution, a wash and then resuspended in FACS buffer to be analyzed via flow cytometry. T cell proliferation was assessed using the CellTrace Violet Proliferation Kit (Thermo Fisher Scientific) per manufacturer's instructions. Prior to seeding, naive OTII cells were incubated for 20 minutes with the CellTrace solution in PBS and then washed in 1X PBS with 1% BSA. Following co-culture, OTII cells were washed with PBS, stained for CD4 and assessed via flow cytometry.

Cell sorting—_For plate-based, full-length scRNA-seq,_ FACS (Astrios) was used to sort one single cell into each well of a 96-well PCR plate containing 5μl of TCL buffer with 1% 2- mercaptoethanol. The cells were stained for 7AAD⁻ (Life Technologies), CD45⁻ (eBioscience), CD31⁻ (eBioscience), Ter119⁻ (eBioscience), EpCAM⁺ (eBioscience), and for specific epithelial cells were also stained for $CD24^{+/-}$ (eBioscience) and $c\text{-}Kit^{+/-}$ (eBioscience). To enrich for specific IEC populations, cells were isolated from Lgr5-GFP mice, stained with the antibodies mentioned above and gated for GFP-high (stem cells), GFP-low (TAs), $GFP^-/CD24^{+/-}/c\text{-}Kit^{+/-}$ (secretory lineages) or $EpCAM^+$ (epithelial cells). A population control of 200 cells was sorted into one well and a nocell control was sorted into another well. After sorting, the plate was sealed tightly with a Microseal F and centrifuged at 800g for 1 min. The plate was immediately frozen on dry ice and kept at −80°C until ready for the lysate cleanup. Bulk population cells were sorted into an Eppendorf tube containing 100μl solution of TCL with 1% 2-mercaptoethanol and stored at −80°C.

For droplet-based scRNA-seq, cells were sorted with the same parameters as described for plate-based scRNA-seq, but into an Eppendorf tube containing 50μl of 1X PBS with 0.4% BSA and stored on ice until proceeding to the GemCode Single Cell Platform or the Chromium Single Cell 3' Library.

Plate-based scRNA-seq—Libraries were prepared using a modified SMART-Seq2 protocol as previously reported (Picelli et al., 2014). RNA lysate cleanup was performed using RNAClean XP beads (Agencourt), followed by reverse transcription with Maxima Reverse Transcriptase (Life Technologies) and whole transcription amplification (WTA) with KAPA HotStart HIFI 2× ReadyMix (Kapa Biosystems) for 21 cycles. WTA products were purified with Ampure XP beads (Beckman Coulter), quantified with Qubit dsDNA HS Assay Kit (ThermoFisher), and assessed with a high sensitivity DNA chip (Agilent). RNA-seq libraries were constructed from purified WTA products using Nextera XT DNA Library Preparation Kit (Illumina). On each plate, the population and no-cell controls were processed using the same method as the single cells. The libraries were sequenced on an Illumina NextSeq 500.

Droplet-based scRNA-seq—Single cells were processed through the GemCode Single Cell Platform per manufacturer's recommendations using the GemCode Gel Bead, Chip and Library Kits (V1) or single cell suspensions were loaded onto 3' library chips as per the manufacturer's protocol for the Chromium Single Cell 3' Library (V2) (10X Genomics; PN-120233). Briefly, single cells were partitioned into Gel Beads in Emulsion (GEMs) in the GemCode/Chromium instrument with cell lysis and barcoded reverse transcription of

RNA, followed by amplification, shearing and 5' adaptor and sample index attachment. An input of 6,000 single cells was added to each channel with a recovery rate of roughly 1,500 cells. Libraries were sequenced on an Illumina Nextseq 500.

Div-Seq—Lgr5-GFP mice were intraperitoneally (IP) injected with 100 mg kg^{-1} EdU from Click-iT Plus EdU Pacific Blue Flow Cytometry Assay Kit (Thermo Fisher Scientific) for 2 hours and then sacrificed. Crypts were isolated as described above and Lgr5$^+$ cells were FACS sorted into PBS, spun down to remove the supernatant, flash frozen and stored in −80°C. Nuclei were isolated using EZ Prep NUC-101 (Sigma) per manufacturer's recommendation, and then incubated in the Click-iT Cocktail per manufacturer's recommendations for 30 min, washed in 1X PBS with 1% BSA and counterstained with Vybrant DyeCyle Ruby stain (Thermo Fisher Scientific) for 15 min. Nuclei were then individually sorted into the wells of 96 well plates with TCL+1% 2-mercaptoethanol as previously described (Habib et al., 2016) using FACS, based on positive Ruby and either EdU^{high} or EdU^{low}.

Plate-based single-nucleus RNA-seq (snRNA-Seq) was then performed as described above for scRNA-seq.

Immunofluorescence and single-molecule fluorescence *in situ* hybridization tsmFISH)

<u>Immunofluorescence (IFA) and immunohistochemistiy (IHC).:</u> Staining of small intestinal tissue was conducted as previously described (Biton et al., 2011). Tissues were fixed for 14 hours in formalin, embedded in paraffin and cut into 5 μm thick sections. Sections were deparaffinized with standard techniques, incubated with primary antibodies overnight at 4°C, and then incubated with secondary antibodies at room temperature for 30 min. Slides were mounted with Slowfade Mountant+DAPI (Life Technologies, S36964) and sealed for IFA, or treated with hematoxylin, dehydrated and mounted for IHC.

<u>Single-molecule fluorescence in situ hybridization (smFISH).:</u> RNAScope Fluorescent Multiplex and RNAScope Multiplex Fluorescent v2 (Advanced Cell Diagnostics) were used per manufacturer's recommendations with the following alterations. Target Retrieval boiling time was adjusted to 12 minutes and incubation with Protease IV at 40°C was adjusted to 8 minutes. Slides were mounted with Slowfade Mountant+DAPI (Life Technologies, S36964) and sealed.

Combined IFA and smFISH was implemented by first performing smFISH, as described above, with the following alterations. After Amp 4, tissue sections were washed in washing buffer, incubated with primary antibodies overnight at 4°C, washed in 1x TBST 3 times and then incubated with secondary antibodies for 30 min at room temperature. Slides were mounted with Slowfade Mountant+DAPI (Life Technologies, S36964) and sealed.

Image analysis—Images of tissue sections were taken with a confocal microscope Fluorview FV1200 using Kalman and sequential laser emission to reduce noise and signal overlap. Scale bars were added to each image using the confocal software FV10-ASW 3.1 Viewer. Images were overlaid and visualized using ImageJ software (Schneider et al., 2012).

Two-photon intra-vital microscopy (2P-IVM) of T cells and Lgr5⁺ ISCs—To generate gut-homing T cells visualized by 2P-IVM, a combination of modified protocols (Esplugues et al., 2011; Iwata et al., 2004) was used. CD4⁺ T cells were isolated from spleen, pLN and mLN from β-actin-RFP mice using a MACS CD4 T cell positive-selection kit (Miltenyi clone L3T4) following the manufacturer's instructions. Plates were pre-treated with 5 μg/mL anti-CD3 (clone 145-201) and 1 μg/mL anti-CD28 (clone 37.51) and 1×10^6 CD4⁺ T cells were added to each well for a final volume of 2.5mL in complete RPMI1640 media supplemented with all-trans Retinoic Acid (100nM, Sigma R2625). The T cells were cultured for 96 hours before replacing half of the volume with fresh media containing 20U/mL of rIL-2 and then cultured for another 48 hours. Before adoptive transfer into Lgr5-GFP hosts, the gut-homing phenotype was validated with flow cytometry for α4β7 and CCR9 expression. 1×10^7 cells were then transferred into recipient mice for two hours, and treated with 20ug of anti-CD3 (clone 2C11). 2P-IVM was performed 72 hours following transfer. The small intestine was surgically exposed through a laparotomy incision. Anesthetized mice were placed on a custom-built stage with a loop of the intact small intestine fixed to a temperature-controlled metallic support to facilitate exposure of the serosal aspect to a water-immersion 20X objective (0.95 numerical aperture) of an upright microscope (Prairie Technologies). A Mai Tai Ti: sapphire laser (Spectra-Physics) was tuned between 870nm and 900nm for multiphoton excitation and second-harmonic generation. For dynamic analysis of cell interaction in four dimensions, several X/Y sections (512×512) with Z spacing ranging from 2μm to 4μm were acquired every 15-20 seconds with an electronic zoom varying from 1X to 3X. Emitted light and second-harmonic signals were directed through 450/80-nm, 525/50-nm and 630/120-nm band-pass filters and detected with non-descanned detectors. Post-acquisition image analysis, volume-rendering and fourdimensional time-lapse videos were performed using Imaris software (Bitplane scientific software).

QUANTIFICATION AND STATISTICAL ANALYSIS

Image quantification

Quantification of proliferating stem cells.: Combined IFA and smFISH images of wild-type C57BL/6J small intestinal tissues were assessed by staining for E-Cadherin to mark cell borders, the canonical proliferation marker *mKi67,* and either the common ISC marker *Lgr5,* our predicted 1cISC markers (*Cyp2e1* or *Fgfr4*) or our predicted hcISC markers (*Psrc1* or *Cenpf*). A line was drawn to establish the bottom of the crypt, termed "stem cell zone", and quantification was only assessed within that zone. For each ISC subset marker, more than 10 randomly chosen intact crypts were analyzed. Cells were examined by double blind quantification and were determined double positive if they co-expressed *mKi67* and one of the ISC subset markers. Proliferating cells in each ISC subset was measured by calculating the fraction of double positive cells out of all cells positive for the specific ISC subset marker.

Automated quantification of Lsr5 mRNA molecules in smFISH images of intestinal crypts within different mouse models was performed using simple bright 'blob' detection implemented a custom Python script.

Pre-processing of plate-based scRNA-seq data—BAM files were converted to merged, de-multiplexed FASTQs using the Illumina provided Bcl2Fastq software package v2.17.1.14. Paired-end reads were mapped to the UCSC mmlO mouse transcriptome using Bowtie (Langmead et al., 2009) with parameters '-q --phred33-quals -n 1 -e 99999999 -1 25 -I 1 -X 2000 -a -m 15 -S -p 6', which allows alignment of sequences with one mismatch. Expression levels of genes were quantified as transcript-per-million (TPM) values calculated by RSEM v1.2.3 in paired-end mode. For each cell, we quantified the number of genes for which at least one read was mapped, and then excluded all cells with either fewer than 3,000 detected genes or a transcriptome-mapping rate of less than 40%.

Selection of variable genes was performed by fitting a generalized linear model to the relationship between the squared coefficient of variation (CV) and the mean expression level in log/log space, and selecting genes that significantly deviated (p<0.05) from the fitted curve, as previously described (Brennecke et al., 2013).

Pre-processing of droplet-based scRNA-seq data—De-multiplexing, alignment to the mm10 mouse transcriptome and UMI-collapsing were performed using the Cellranger toolkit (version 1.0.1) provided by 10X Genomics. For each cell, we quantified the number of genes for which at least one read was mapped, and then excluded all cells with fewer than 800 detected genes. In analyzing CD45^{+} immune cells, we excluded all cells with fewer than 250 detected genes. Expression values $E_{i,j}$ for gene i in cell j were calculated by dividing UMI count values for gene i by the sum of the UMI counts in cell j, to normalize for differences in coverage, and then multiplying by 10,000 to create TPM-like values, and finally calculating $\log_2(\text{TPM}+1)$ values. Batch correction was performed using ComBat (Johnson et al., 2007) as implemented in the R package sva using the default parametric adjustment mode. The output was a corrected expression matrix, which was used as input to further analysis. We identified highly variable genes as described above.

Dimensionality reduction by PCA—We restricted the expression matrix to the subsets of variable genes and high-quality cells noted above, and values were centered and scaled before input to PCA, which was implemented using the R function 'prcomp' from the 'stats' package for the plate-based dataset. For the droplet-based data, we used a randomized approximation to PCA, implemented using the 'rpca' function from the 'rsvd' R package, with the parameter k set to 100. This low-rank approximation is several orders of magnitude faster to compute for very wide matrices. After PCA, significant PCs were identified using a permutation test as previously described (Buja and Eyuboglu, 1992), implemented using the 'permutationPA' function from the 'jackstraw' R package. Only scores from these significant PCs were used as the input to further analysis.

tSNE visualization—For visualization purposes only (and *not* for clustering), dimensionality was further reduced using the Barnes-Hut approximate version of the *t*-distributed stochastic neighbor embedding (tSNE) (van der Maaten, 2014). This was implemented using the 'Rtsne' function from the 'Rtsne' R package using 20,000 iterations and a perplexity setting that ranged from 10 to 30 depending on the size of the dataset. Scores from the first n PCs were used as the input to tSNE, where n was determined for each dataset using the permutation test described above.

Removing doublets—In the plate-based dataset, several cells were outliers in terms of library complexity, which could possibly correspond to more than one individual cell per sequencing library, or 'doublets'. As a precaution, we removed any cells in the top quantile 1% of the distribution of genes detected per cell, as these may correspond to doublets.

***k*-NN graph-based clustering—**To cluster single cells by their expression profiles, we used unsupervised clustering, based on the Infomap graph-clustering algorithm (Rosvall and Bergstrom, 2008). Briefly, we constructed a *k* nearest neighbor (*k*-NN) graph on the data using as the metric for each pair of cells, the distance between the scores of significant PCs. The parameter *k* was chosen in a manner roughly consistent with the size of the dataset (Table S2). Specifically, *k* was set to 600, 200 and 50 for the droplet dataset of 23,177, 4,332 and 1,090 cells from combined T cell and cytokines, IL-13-treated and Th1 co-cultured organoids, respectively. For *in vivo* mouse models, *k* was set to 100, 300, 175, and 100 for nude mice, TCRβ KO, Foxp3-DTR and MHCII ^{gut} respectively. For subclustering of stem cell subsets, we used *k*=150 and *k*=40 for the 637. The combined *Salmonella* and *H. polygyrus* infection dataset contained 5,122 immune cells and *k* was set to 200. The *k*-NN graph was computed using the function 'nng' from the R package 'cccd' and was then used as the input to Infomap (Rosvall and Bergstrom, 2008), implemented using the 'infomap.community' function from the 'igraph' R package. For *k*-NN graph-based clustering of the 24,649 CD45$^+$ immune cells, the 'FindClusters' function from R package 'Seurat' was used with the resolution parameter set to 1.

Detected clusters were annotated by cell types or states using known markers for IEC subtypes (Sato et al., 2009). Specifically, for each known epithelial type we selected five canonical marker genes (*e.g., Lgr5, Ascl2, Slc12a2, Axin2* and *Olfm4* for stem cells, or *Lyz1, Defa17, Defa22, Defa24* and *Aug4* for Paneth cells), and scored all clusters for their expression (see below for signature scoring procedure). In all cases, one cluster unambiguously expressed each cell-type signature, with two exceptions: in the plate-based dataset, two clusters both expressed high levels of Lgr5$^+$ ISC markers and accordingly were merged to form a 'Stem' cluster and two other clusters were merged to form a 'TA' cluster based on high expression of cell-cycle genes and low-to-moderate expression of Lgr5$^+$ ISC genes. In the case of the CD45$^+$ immune cells, the following markers were used to interpret clusters *post hoc.* B cells: *Bank1, Fcer2a, Cd79a, Cd79b, Cd22.* B cell (cycling): *Mki67, Cd79a, Cd79b, Ms4a1, Pou2af1.* Cd4$^+$ T helper cells: *Cd4, Foxp3, Gata3, Cd3g, Tnfrsf4.* Cd8 T cells: *Gzma, Gzmb, Cd8a.* Dendritic cells (DCs): *Itgae, Tlr3, Cd209a, Cd209b, Irf8, H2-Ab1, Clec9a.* Epithelial: *Epcam, Krt8, Vil1, Muc2, Krt20.* Inflammatory monocytes: *Ccr2, Ly6c2, Fcgr1, Ifitm3, Fn1.* Neutrophils: *S100a9, S100a8, Csf3r, Cxcr2, Msrb1, Ccrl2.* Natural Killer (NK) cells: *Ncr1, Prf1, Klra1, Xcl1.* Plasmacytoid dendritic cells: *Siglech, Bst2, Tlr7.* Plasma cell: *Jchain, Mzb1, Xbp1, Sdc1.*

Assigning the three Lgr5$^+$ISC states to region of origin using supervised classification—To study the anatomical distribution of ISCs in different parts of the small intestine, we used a classification approach. First, we developed a classifier for the anatomical origin of Lgr5$^+$ ISCs using single-cell expression profiles of 2,965 ISCs extracted from duodenum, jejunum and ileum (Haber et al., 2017), by compiling a

discriminative feature set using the expression levels of all genes differentially expressed (FDR < 0.1, Mann-Whitney U-test, $\log_2$ fold-change > 0.25) between stem cells from the three regions, and also the scores along the first 25 PCs. A 'random forest' classifier was trained on these features, and subsequently distinguished between Lgr5+ ISCs from the three regions with an average out-of-bag accuracy of 92.9%. Finally, we used the trained classifier to classify the 637 ISCs (Figure 1) and infer the fraction of cells drawn from each intestinal region found in each ISC state (Figure S1F).

Cell-cell similarity matrix—To visualize heterogeneity of Lgr5+ ISCs within the 'Stem' cluster (637 cells), cell-cell similarities were computed. Principal component (PC) scores for each cell were computed across the 637 cells using the R function 'prcomp' as described above. The distance between cell i and j was calculated as the Pearson correlation between the scores of these two cells along the first 10 PCs. This distance matrix was then ordered using the k-NN graph-based cluster assignments described above, and visualized as a heatmap using the R function 'aheatmap'.

Cell-cycle and Lgr5+ ISC subset signatures—To identify maximally specific genes associated with the three ISC subsets, we performed differential expression tests between each possible pairwise comparison between clusters. To ensure specificity of the detected marker genes to stem cells, the set of clusters included both the three ISC subsets (3 clusters), and all other detected IEC clusters (8 clusters) for a total of 11 clusters. Then, for a given cluster, putative signature genes were filtered using the maximum FDR Q-value and ranked by the minimum $\log_2$(fold-change). The minimum fold-change and maximum Q-value represents the weakest effect-size across all pairwise comparisons, therefore this is a stringent criterion. Lgr5+ ISC subset signatures (Table S1) were obtained using a maximum FDR of 0.25 and a minimum $\log_2$(fold-change) of 0.25. To exclude the explicit effect of known cell-cycle genes on the gene signature of the ISC subsets we filtered out any gene annotated as directly participating in cell-cycle regulation. Annotated cell-cycle genes were downloaded from the gene ontology(GO):http://amigo.geneontology.org/amigo/term/GO: 0007049. and any gene appearing on this list was removed from the signature gene sets.

Gene sets associated with G1/S and G2/M phases of the cell-cycle were downloaded from http://www.cell.com/cms/attachment/2051395126/2059328514/mmc2.xlsx (Macosko et al.. 2015), A set of cell-cycle genes to assess overall proliferation (see below for scoring procedure) was defined as the union of the G1/S and G2/M sets.

Scoring cells using signature gene sets—To score a specific set of n genes in a given cell, a 'background' gene set was defined to control for differences in sequencing coverage and library complexity between cells (Kowalczyk et al., 2015). The background gene set was selected to be similar to the genes of interest in terms of expression level. Specifically, the $10n$ nearest gene neighbors in the 2-D space defined by mean expression and detection frequency across all cells were selected. The signature score for that cell was then defined as the mean expression of the n signature genes in that cell, minus the mean expression of the $10n$ background genes in that cell.

Pseudo-time analysis of stem and progenitor cell differentiation—We used diffusion maps (Haghverdi et al., 2015) to order both *in vivo* stem and progenitor cells and the organoid IECs according to their differentiation state. For *in vivo* IECs, diffusion maps were computed for all cells together. In the case of organoids, for each of the two cytokines with the strongest effect on the stem cell pool (IL-10 and IL-13; Figure 2D), we build independent diffusion maps, along with their matched control organoids, using the function 'DiffusionMap' from the R package 'destiny', using only a set of highly variable genes that were selected as described above.

Since the major source of variability amongst these cells was differentiation, we reasoned that diffusion pseudotime would likely reflect the progression along an axis from stem to mature IECs. Specifically, the diffusiopseudotime is a relative metric and measures the distance between each cell and a specified root cell. We use the intestinal stem cell as the root since it is a natural starting point from which to measure developmental progression. As there is only a single pseudotime axis, this represents development progress across multiple trajectories and reflects the stem-differentiation axis in general (rather than branching to specific lineages). Indeed, for organoids, there was a high correlation between pseudotime n (calculated using the function 'DPT'), and a stemness signature score, computed using 10 known $Lgr5^+$ ISC markers (as in Figure S1A,I) (Spearman $|\rho|$ 0.70 for IL-10 and $|\rho|$ 0.66 for IL-13, $p<2* 10^{-16}$ in both cases). We performed a further optimization step by varying the diffusion map's Gaussian kernel width parameter (σ), and selecting the value that maximized ρ in each case. The resulting values were σ=8 for both IL-10 and IL-13.

For *in vivo* IECs, diffusion component 1 (DC-1) was strongly correlated with the expression of the stemness signature score (r=0.83, Figure S1I), and the score of each cell along DC-1 was therefore selected as the pseudotime axis. In all cases, the significance of differences in the distribution of cells along the pseudo-time axis were computed using the Mann-Whitney U-test.

Testing for shifts in cell proportions in intestinal organoids—Under several conditions, we observed dramatic changes in the frequency of epithelial cell subtypes. The statistical significance of these shifts was assessed by calculating, for each condition comparison and cell type, the exact hypergeometric probability (without replacement) of the observed change in cell numbers.

Specifically, given that **m** and **n** total cells (of all cell types) are sequenced in a treatment and control condition respectively, we test, for a given cell type, whether the number of **k** and **q** of observed cells of type *C* in total and treatment condition respectively, significantly deviates from a null model given by the hypergeometric distribution. The probability of observing these values was calculated using the R function 'phyper' from the 'stats' package, using the command: P = phyper(q, k, m, n) and was reported as a hyper geometric *p*-value. Confidence intervals for the odds-ratio were computed using the R function 'fisher.test'.

Testing for shifts in cell proportions *in vivo*—In the case of *in vivo* perturbation experiments, we used a regression model to control for any mouse-to-mouse variability

amongst our biological replicates. For each cell-type, we model the number of cells detected in each analyzed mouse as a random count variable using a negative binomial distribution. The rate of detection (as a fraction of all cells) is then modeled by using the natural log of the total number of cells profiled in a given mouse as an offset variable. The genotype of each mouse (*i.e.*, knock-out or wild-type) was provided as a covariate. The model was fit using the R command 'glm.nb' from the 'MASS' package. The *p*-value for the significance of the effect produced by the knock-out was then assessed using a likelihood-ratio test computed using the R function 'anova'.

GO analysis—GO analysis was performed using the 'goseq' R package (Young et al., 2010), using significantly differentially expressed genes (FDR <0.05) as target genes, and all genes expressed with $\log_2(\text{TPM}+1) > 3$ in at least 10 cells as background.

Analysis of CD4$^+$ T helper cell activation in MHC$^{\text{gut}-/-}$ mice—Differential expression analysis of 1,150 CD4$^+$ T helper cells (Table S5) under homeostasis was conducted using the 'MAST' R package, and the up-regulated genes (FDR < 0.01, likelihood-ratio test and $\log_2$ fold-change > 0.1) were tested for enrichment among the 495 genes in the 'T cell activation' GO term (G0:0042110) by the hypergeometric test using the R function 'fisher.test'. We note that due to the lower numbers of CD4$^+$ T helper cells in the *H. polygyrus* condition, the same DE test revealed no differentially expressed genes between the MHC$^{\text{gut}-/-}$ and matched controls.

As a confirmatory analysis, we also scored (using the procedure described above) the CD4$^+$ Th cells from all conditions for set of 13 canonical T cell activation markers: *Cd28, Cd40lg, Cd44, Cd69, Ctla4, Dpp4* (CD26), *Havcr2* (TIM-3), *Icos, Il2ra* (CD25), *Lag3, Pdcd1* (PD1), *Tfrc* (CD71) and *Tigit,* and tested for differences in the signature score between conditions using the Mann-Whitney U-test.

DATA AND SOFTWARE AVAILABILITY

All raw and processed single-cell RNA sequencing data generated for this study have been deposited in the NCBI Gene Expression Omnibus (GEO) under ID code GSE106510.

Python code for mRNA quantification from smFISH images can be found in the following repository: https://github.com/adamh-broad/image_analysis.

Raw data can be found in Mendeley: https://data.mendeley.com/datasets/9rvb5p2vdh/edit

ADDITIONAL RESOURCES

Single Cell Portal (https://portals.broadinstitute.org/single_cell/intestinal_stem_cell)

Supplementary Material

Refer to Web version on PubMed Central for supplementary material.

Acknowledgements

References

Agudo J, Park ES, Rose SA, Alibo E, Sweeney R, Dhainaut M, Kobayashi KS, Sachidanandam R, Baccarini A, Merad M, et al. (2018). Quiescent Tissue Stem Cells Evade Immune Surveillance. Immunity 48, 271–285 e275. [PubMed: 29466757]

Ali N, Zirak B, Rodriguez RS, Pauli ML, Truong HA, Lai K, Ahn R, Corbin K, Lowe MM, Scharschmidt TC, et al. (2017). Regulatory T Cells in Skin Facilitate Epithelial Stem Cell Differentiation. Cell 169, 1119–1129 e1111. [PubMed: 28552347]

Anthony RM, Rutitzky LI, Urban JF, Jr., Stadecker MJ, and Gause WC (2007). Protective immune mechanisms in helminth infection. Nature reviews Immunology 7, 975–987.

Arpaia N, Green JA, Moltedo B, Arvey A, Hemmers S, Yuan S, Treuting PM, and Rudensky AY (2015). A Distinct Function of Regulatory T Cells in Tissue Protection. Cell 162, 1078–1089. [PubMed: 26317471]

Aurora AB, and Olson EN (2014). Immune modulation of stem cells and regeneration. Cell Stem Cell 15, 14–25. [PubMed: 24996166]

Barker N, van Es JH, Kuipers J, Kujala P, van den Born M, Cozijnsen M, Haegebarth A, Korving J, Begthel H, Peters PJ, et al. (2007). Identification of stem cells in small intestine and colon by marker gene Lgr5. Nature 449, 1003–1007. [PubMed: 17934449]

Beyaz S, Mana MD, Roper J, Kedrin D, Saadatpour A, Hong SJ, Bauer-Rowe KE, Xifaras ME, Akkad A, Arias E, et al. (2016). High-fat diet enhances stemness and tumorigenicity of intestinal progenitors. Nature 531, 53–58. [PubMed: 26935695]

Biton M, Levin A, Slyper M, Alkalay I, Horwitz E, Mor H, Kredo-Russo S, Avnit-Sagi T, Cojocaru G, Zreik F, et al. (2011). Epithelial microRNAs regulate gut mucosal immunity via epithelium-T cell crosstalk. Nat Immunol 12, 239–246. [PubMed: 21278735]

Bland PW, and Warren LG (1986). Antigen presentation by epithelial cells of the rat small intestine. I. Kinetics, antigen specificity and blocking by anti-Ia antisera. Immunology 58, 1–7. [PubMed: 2423435]

Brennecke P, Anders S, Kim JK, Kołodziejczyk AA, Zhang X, Proserpio V, Baying B, Benes V, Teichmann SA, Marioni JC, et al. (2013). Accounting for technical noise in single-cell RNA-seq experiments. Nature Methods 10, 1093–1095. [PubMed: 24056876]

Buczacki SJ, Zecchini HI, Nicholson AM, Russell R, Vermeulen L, Kemp R, and Winton DJ (2013). Intestinal label-retaining cells are secretory precursors expressing Lgr5. Nature 495, 65–69. [PubMed: 23446353]

Buja A, and Eyuboglu N (1992). Remarks on Parallel Analysis. Multivariate Behavioral Research 27, 509–540. [PubMed: 26811132]

Burzyn D, Kuswanto W, Kolodin D, Shadrach JL, Cerletti M, Jang Y, Sefik E, Tan TG, Wagers AJ, Benoist C, et al. (2013). A special population of regulatory T cells potentiates muscle repair. Cell 155, 1282–1295. [PubMed: 24315098]

Chinen T, Volchkov PY, Chervonsky AV, and Rudensky AY (2010). A critical role for regulatory T cell-mediated control of inflammation in the absence of commensal microbiota. J Exp Med 207, 2323–2330. [PubMed: 20921284]

Cordier AC, and Haumont SM (1980). Development of thymus, parathyroids, and ultimo-branchial bodies in NMRI and nude mice. Am J Anat 157, 227–263. [PubMed: 7405870]

Degirmenci B, Valenta T, Dimitrieva S, Hausmann G, and Basler K (2018). GLI1-expressing mesenchymal cells form the essential Wnt-secreting niche for colon stem cells. Nature.

Denning TL, Campbell NA, Song F, Garofalo RP, Klimpel GR, Reyes VE, and Ernst PB (2000). Expression of IL-10 receptors on epithelial cells from the murine small and large intestine. Int Immunol 12, 133–139. [PubMed: 10653848]

el Marjou F, Janssen KP, Chang BH, Li M, Hindie V, Chan L, Louvard D, Chambon P, Metzger D, and Robine S (2004). Tissue-specific and inducible Cre-mediated recombination in the gut epithelium. Genesis 39, 186–193. [PubMed: 15282745]

Esplugues E, Huber S, Gagliani N, Hauser AE, Town T, Wan YY, O'Connor W, Jr., Rongvaux A, Van Rooijen N, Haberman AM, et al. (2011). Control of TH17 cells occurs in the small intestine. Nature 475, 514–518. [PubMed: 21765430]

Farin HF, Karthaus WR, Kujala P, Rakhshandehroo M, Schwank G, Vries RG, Kalkhoven E, Nieuwenhuis EE, and Clevers H (2014). Paneth cell extrusion and release of antimicrobial products is directly controlled by immune cell-derived IFN-gamma. J Exp Med 211, 1393–1405. [PubMed: 24980747]

Gerbe F, Sidot E, Smyth DJ, Ohmoto M, Matsumoto I, Dardalhon V, Cesses P, Gamier L, Pouzolles M, Brulin B, et al. (2016). Intestinal epithelial tuft cells initiate type 2 mucosal immunity to helminth parasites. Nature 529, 226–230. [PubMed: 26762460]

Grim D, Lyubimova A, Kester L, Wiebrands K, Basak 0, Sasaki N, Clevers H, and van Oudenaarden A (2015). Single-cell messenger RNA sequencing reveals rare intestinal cell types. Nature, 1–23.

Haber AL, Biton M, Rogel N, Herbst RH, Shekhar K, Smillie C, Burgin G, Delorey TM, Howitt MR, Katz Y, et al. (2017). A single-cell survey of the small intestinal epithelium. Nature 551, 333–339. [PubMed: 29144463]

Habib N, Li Y, Heidenreich M, Swiech L, Avraham-Davidi I, Trombetta JJ, Hession C, Zhang F, and Regev A (2016). Div-Seq: Single-nucleus RNA-Seq reveals dynamics of rare adult newborn neurons. Science 353, 925–928. [PubMed: 27471252]

Haghverdi L, Buettner F, and Theis FJ (2015). Diffusion maps for high-dimensional single-cell analysis of differentiation data. Bioinformatics 31, 2989–2998. [PubMed: 26002886]

Hashimoto K, Joshi SK, and Koni PA (2002). A conditional null allele of the major histocompatibility IA-beta chain gene. Genesis 32, 152–153. [PubMed: 11857806]

Howie D, Garcia Rueda H, Brown MH, and Waldmann H (2013). Secreted and transmembrane 1A is a novel co-stimulatory ligand. PLoS One 8, e73610. [PubMed: 24039998]

Howitt MR, Lavoie S, Michaud M, Blum AM, Tran SV, Weinstock JV, Gallini CA, Redding K, Margolskee RF, Osborne LC, et al. (2016). Tuft cells, taste-chemosensory cells, orchestrate parasite type 2 immunity in the gut. Science 351, 1329–1333. [PubMed: 26847546]

Iwata M, Hirakiyama A, Eshima Y, Kagechika H, Kato C, and Song SY (2004). Retinoic acid imprints gut-homing specificity on T cells. Immunity 21, 527–538. [PubMed: 15485630]

Jager A, Dardalhon V, Sobel RA, Bettelli E, and Kuchroo VK (2009). Th1, Th17, and Th9 effector cells induce experimental autoimmune encephalomyelitis with different pathological phenotypes. J Immunol 183, 7169–7177. [PubMed: 19890056]

Johnson WE, Li C, and Rabinovic A (2007). Adjusting batch effects in microarray expression data using empirical Bayes methods. Biostatistics (Oxford, England) 8, 118–127.

Kaiserlian D, Vidal K, and Revillard JP (1989). Murine enterocytes can present soluble antigen to specific class II-restricted CD4+ T cells. Eur J Immunol 19, 1513–1516. [PubMed: 2570703]

Kim JM, Rasmussen JP, and Rudensky AY (2007). Regulatory T cells prevent catastrophic autoimmunity throughout the lifespan of mice. Nat Immunol 8, 191–197. [PubMed: 17136045]

Kowalczyk MS, Tirosh I, Heckl D, Rao TN, Dixit A, Haas BJ, Schneider RK, Wagers AJ, Ebert BL, and Regev A (2015). Single-cell RNA-seq reveals changes in cell cycle and differentiation programs upon aging of hematopoietic stem cells. Genome Research 25, 1860–1872. [PubMed: 26430063]

Langmead B, Trapnell C, Pop M, and Salzberg SL (2009). Ultrafast and memory-efficient alignment of short DNA sequences to the human genome. Genome Biology.

Lindemans CA, Calafiore M, Mertelsmann AM, O'Connor MH, Dudakov JA, Jenq RR, Velardi E, Young LF, Smith OM, Lawrence G, et al. (2015). Interleukin-22 promotes intestinal-stem-cell-mediated epithelial regeneration. Nature 528, 560–564. [PubMed: 26649819]

Mabbott NA, Donaldson DS, Ohno H, Williams IR, and Mahajan A (2013). Microfold (M) cells: important immunosurveillance posts in the intestinal epithelium. Mucosal Immunol 6, 666–677. [PubMed: 23695511]

Macosko EZ, Basu A, Satija R, Nemesh J, Shekhar K, Goldman M, Tirosh I, Bialas AR, Kamitaki N, Martersteck EM, et al. (2015). Highly Parallel Genome-wide Expression Profiling of Individual Cells Using Nanoliter Droplets. Cell 161, 1202–1214. [PubMed: 26000488]

Madison BB, Dunbar L, Qiao XT, Braunstein K, Braunstein E, and Gumucio DL (2002). Cis elements of the villin gene control expression in restricted domains of the vertical (crypt) and horizontal (duodenum, cecum) axes of the intestine. J Biol Chem 277, 33275–33283. [PubMed: 12065599]

Madsen L, Labrecque N, Engberg J, Dierich A, Svejgaard A, Benoist C, Mathis D, and Fugger L (1999). Mice lacking all conventional MHC class II genes. Proc Natl Acad Sci U S A 96, 10338–10343. [PubMed: 10468609]

Mombaerts P, Clarke AR, Rudnicki MA, Iacomini J, Itohara S, Lafaille JJ, Wang L, Ichikawa Y, Jaenisch R, Hooper ML, et al. (1992). Mutations in T-cell antigen receptor genes alpha and beta block thymocyte development at different stages. Nature 360, 225–231. [PubMed: 1359428]

Muñoz J, Stange DE, Schepers AG, van de Wetering M, Koo B-K, Itzkovitz S, Volckmann R, Kung KS, Koster J, Radulescu S, et al. (2012). The Lgr5 intestinal stem cell signature: robust expression of proposed quiescent '+4' cell markers. The EMBO Journal 31, 3079–3091. [PubMed: 22692129]

Nusse YM, Savage AK, Marangoni P, Rosendahl-Huber AKM, Landman TA, de Sauvage FJ, Locksley RM, and Klein OD (2018). Parasitic helminths induce fetal-like reversion in the intestinal stem cell niche. Nature 559, 109–113. [PubMed: 29950724]

Ramilowski JA, Goldberg T, Harshbarger J, Kloppmann E, Lizio M, Satagopam VP, Itoh M, Kawaji H, Carninci P, Rost B, et al. (2015). A draft network of ligand-receptor-mediated multicellular signalling in human. Nat Commun 6, 7866. [PubMed: 26198319]

Rosvall M, and Bergstrom CT (2008). Maps of random walks on complex networks reveal community structure. Proceedings of the National Academy of Sciences 105, 1118–1123.

Rubin DB (1981). The Bayesian bootstrap. The Annals of Statistics 9, 130–134.

Saha S, Aranda E, Hayakawa Y, Bhanja P, Atay S, Brodin NP, Li J, Asfaha S, Liu L, Tailor Y, et al. (2016). Macrophage-derived extracellular vesicle-packaged WNTs rescue intestinal stem cells and enhance survival after radiation injury. Nat Commun 7, 13096. [PubMed: 27734833]

Sato T, van Es JH, Snippert HJ, Stange DE, Vries RG, van den Born M, Barker N, Shroyer NF, van de Wetering M, and Clevers H (2011). Paneth cells constitute the niche for Lgr5 stem cells in intestinal crypts. Nature 469, 415–418. [PubMed: 21113151]

Sato T, Vries RG, Snippert HJ, van de Wetering M, Barker N, Stange DE, van Es JH, Abo A, Kujala P, Peters PJ, et al. (2009). Single Lgr5 stem cells build crypt-villus structures in vitro without a mesenchymal niche. Nature 459, 262–265. [PubMed: 19329995]

Schneider CA, Rasband WS, and Eliceiri KW (2012). NIH Image to ImageJ: 25 years of image analysis. Nat Methods 9, 671–675. [PubMed: 22930834]

Shalek AK, Satija R, Shuga J, Trombetta JJ, Gennert D, Lu D, Chen P, Gertner RS, Gaublomme JT, Yosef N, et al. (2014). Single-cell RNA-seq reveals dynamic paracrine control of cellular variation. Nature 510, 363–369. [PubMed: 24919153]

Shi HN, Koski KG, Stevenson MM, and Scott ME (1997). Zinc deficiency and energy restriction modify immune responses in mice during both primary and challenge infection with Heligmosomoides polygyrus (Nematoda), Parasite Immunol 19, 363–373. [PubMed: 9292895]

Shoshkes-Carmel M, Wang YJ, Wangensteen KJ, Toth B, Kondo A, Massassa EE, Itzkovitz S, and Kaestner KH (2018). Subepithelial telocytes are an important source of Wnts that supports intestinal crypts. Nature 557, 242–246. [PubMed: 29720649]

Stappenbeck TS, and Miyoshi H (2009). The role of stromal stem cells in tissue regeneration and wound repair. Science 324, 1666–1669. [PubMed: 19556498]

Tanoue T, Atarashi K, and Honda K (2016). Development and maintenance of intestinal regulatory T cells. Nature reviews Immunology 16, 295–309.

Tetteh PW, Basak O, Farin HF, Wiebrands K, Kretzschmar K, Begthel H, van den Born M, Korving J, de Sauvage F, van Es JH, et al. (2016). Replacement of Lost Lgr5-Positive Stem Cells through Plasticity of Their Enterocyte-Lineage Daughters. Cell Stem Cell 18, 203–213. [PubMed: 26831517]

Thelemann C, Eren RO, Coutaz M, Brasseit J, Bouzourene H, Rosa M, Duval A, Lavanchy C, Mack V, Mueller C, et al. (2014). Interferon-gamma induces expression of MHC class II on intestinal epithelial cells and protects mice from colitis. PLoS One 9, e86844. [PubMed: 24489792]

Tirosh I, Izar B, Prakadan SM, Wadsworth MH, 2nd, Treacy D, Trombetta JJ, Rotem A, Rodman C, Lian C, Murphy G, et al. (2016). Dissecting the multicellular ecosystem of metastatic melanoma by single-cell RNA-seq. Science 352, 189–196. [PubMed: 27124452]

van der Flier LG, and Clevers H (2009). Stem cells, self-renewal, and differentiation in the intestinal epithelium. Annu Rev Physiol 71, 241–260. [PubMed: 18808327]

van der Maaten L (2014). Accelerating t-SNE using Tree-Based Algorithms. The Journal of Machine Learning Research 15, 3221–3245.

von Moltke J, Ji M, Liang HE, and Locksley RM (2016). Tuft-cell-derived IL-25 regulates an intestinal ILC2-epithelial response circuit. Nature 529, 221–225. [PubMed: 26675736]

Wang T, Huang C, Lopez-Coral A, Slentz-Kesler KA, Xiao M, Wherry EJ, and Kaufman RE (2012). K12/SECTM1, an interferon-gamma regulated molecule, synergizes with CD28 to costimulate human T cell proliferation. J Leukoc Biol 91, 449–459. [PubMed: 22184754]

Yan KS, Janda CY, Chang J, Zheng GXY, Larkin KA, Luca VC, Chia LA, Mah AT, Han A, Terry JM, et al. (2017). Non-equivalence of Wnt and R-spondin ligands during Lgr5+ intestinal stem-cell self-renewal. Nature 545, 238–242. [PubMed: 28467820]

Young MD, Wakefield MJ, Smyth GK, and Oshlack A (2010). Gene ontology analysis for RNA-seq: accounting for selection bias. Genome Biology 11.

Ziegler SF, and Artis D (2010). Sensing the outside world: TSLP regulates barrier immunity. Nat Immunol 11, 289–293. [PubMed: 20300138]

Author Manuscript

Author Manuscript

Author Manuscript

Author Manuscript

Highlights

- Intestinal stem cells (ISCs) are non-conventional antigen presenting cells by MHCII

- Interactions between ISCs and T helper subsets modulate distinct ISC fates

- Epithelial MHCII is important for epithelial cell remodeling following infection

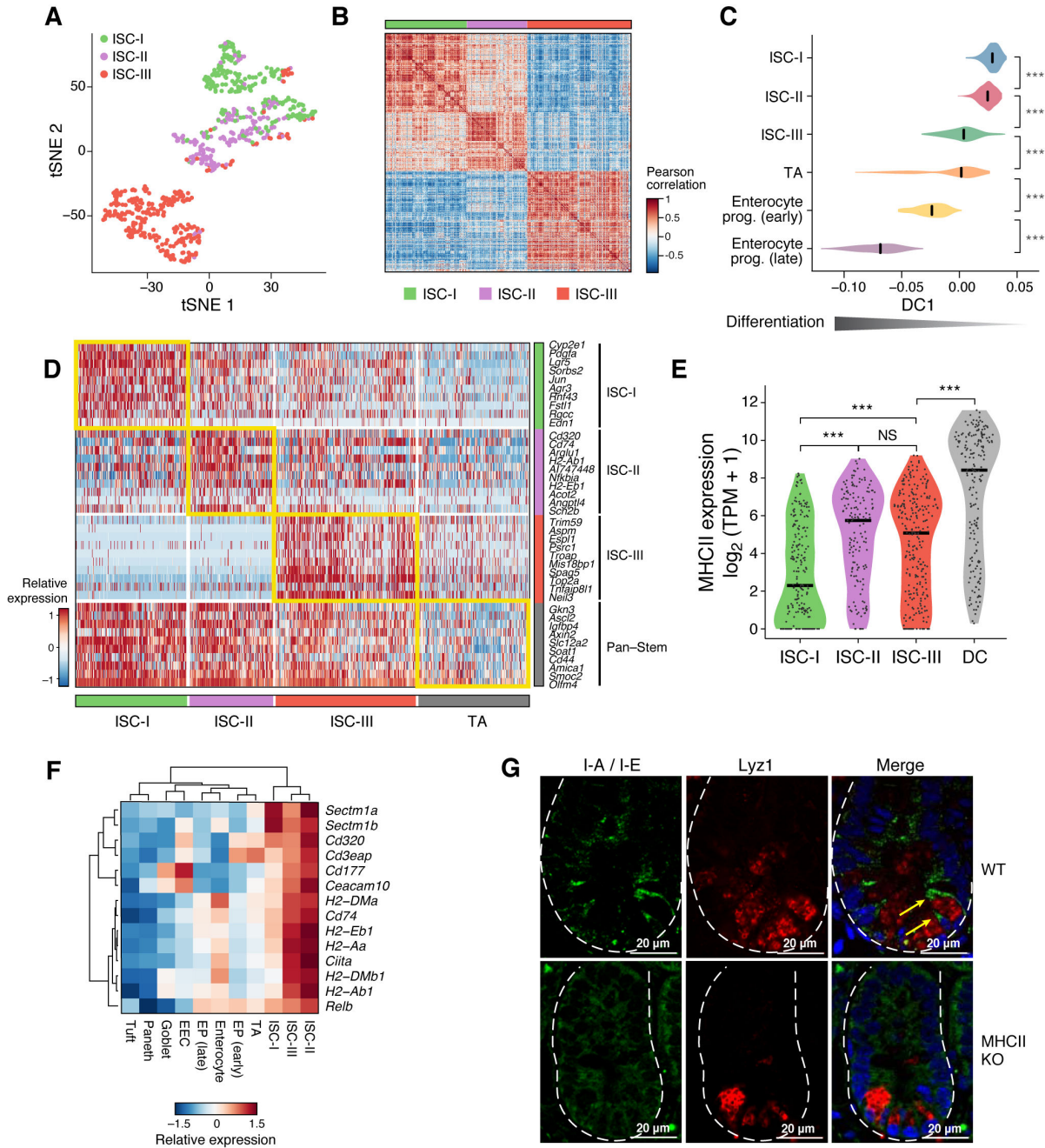- Regulatory T cells and their key cytokine IL-10 support ISC renewal

Figure 1. ScRNA-seq reveals MHCII expression in subsets of *Lgr5*⁺ ISCs.
A,B. Three subsets of Lgr5⁺ ISCs. A *t*-distributed stochastic neighbor embedding (tSNE)
(**A**) and correlation matrix (**B**) of 637 ISCs identified by clustering of 1,522 cells by scRNA-
seq. Color code: *k*NN-graph clusters and *post-hoc* annotation. Heatmap (**B**) shows the
Pearson correlation coefficient (*r*, color bar) between cell scores along the first 10 principal
components. **C.** Differentiation pseudotime of ISC subsets. Distribution of DC-1 scores
("differentiation", x-axis) for each cell cluster (y-axis). Black bar: mean. *** *p<0.0001,*
Mann-Whitney U-test. **D.** Gene signatures of ISC subsets. Relative expression level (row-
wise Z-score of log$_2$(TPM+1) values, color bar) in 637 ISCs and 201 TA (columns, color

code as in **(A)**) of 10 representative genes of ISCs or ISC subsets (rows). **E.** MUCII expression in ISCs. Distributions of mean expression levels ($\log_2$(TPM+1), y-axis) of MHCII genes (STAR Methods) in each ISC subset and dendritic cells (DC) (Shalek et al., 2014). **F.** Enriched MHCII gene expression in ISCs. Relative mean expression (row-wise Z-score of $\log_2$(TPM+1) values, color bar) of MHCII-related genes (rows) in each IEC type (columns). EP: Enterocyte progenitor, EEC: enteroendocrine cell. **G.** MHCII expression *in situ.* IFA co-stain of MHCII (I-A/I-E; green) and the Paneth cell marker Lyzl (red) in intestinal crypts of WT (top) and MHCII KO (bottom) mice. Yellow arrows: MHCII-expressing cells. Scale bar, 20μm.
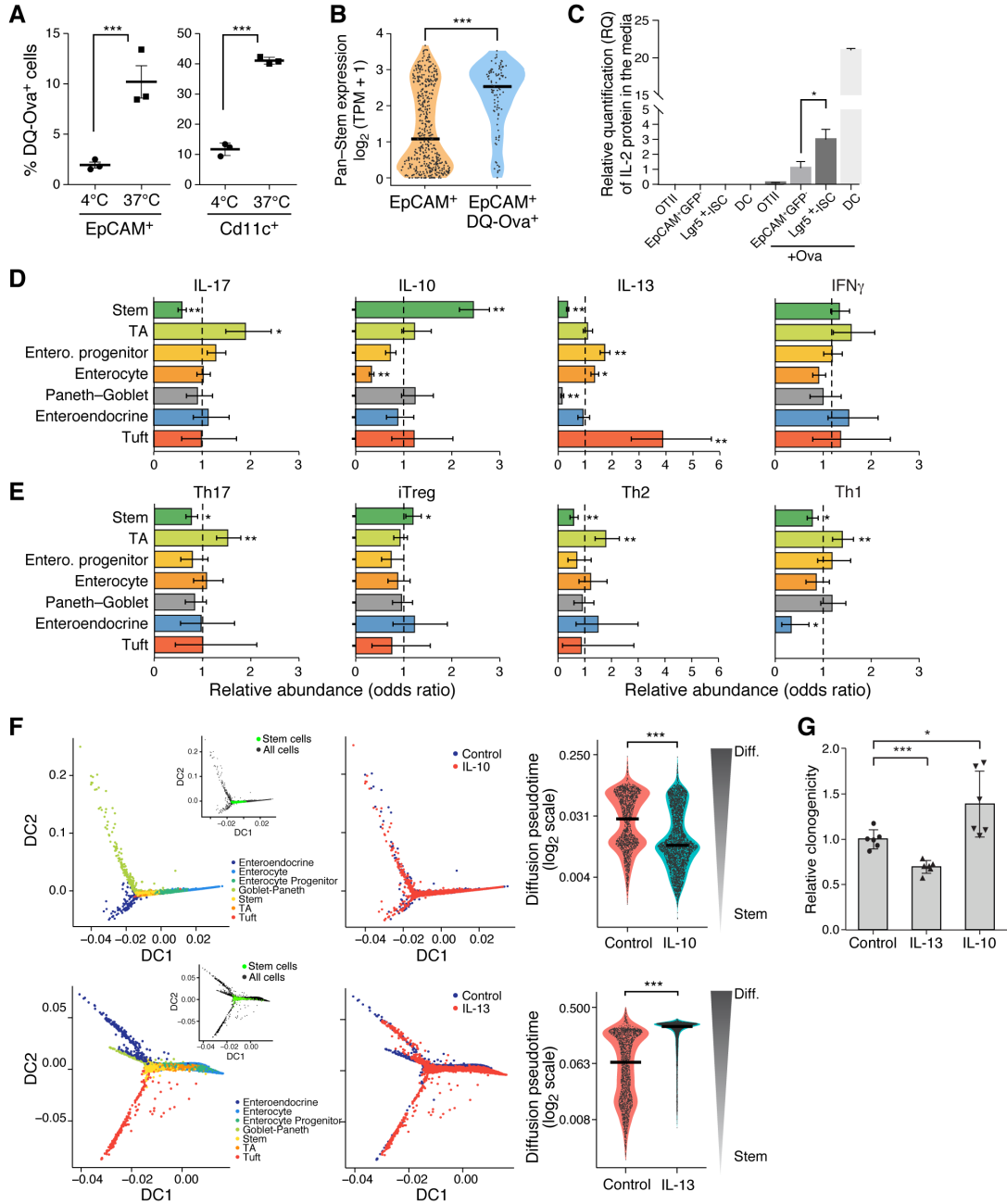
Figure 2. Antigen presentation by ISCs and the impact of Th cytokines on IEC differentiation.
A. IECs process ovalbumin antigen. Proportion of cells positive for DQ-ovalbumin (DQ-Ova) (*y*-axis) among EpCAM^{+} cells (left) and DCs (right) incubated with 10μg of DQ-Ova (*x*-axis). n=3 mice, ***p<0.01, *t*-test, error bars: SEM. **B.** DQ-Ova[+] IECs are enriched for ISCs. Distribution of ISC signature scores in scRNA-seq of EpCAM[+] or EpCAM[+] DQ-Ova^{+} cells (***p<0.001, Wilcoxon test). **C.** Lgr5^{+} ISCs interact with and activate naïve Th cells. Relative quantification (RQ) of IL-2 secreted in the media (*y*-axis) of naïve OTII cells cultured alone or with EpCAM[+]GFP[−], EpCAM[+]GFP[+] (Lgr5^{+} ISC) or DCs with or without 15μg/mL Ova peptide (*n*=9 mice, * *p*<0.05, *t*-test, error bars: SEM). All groups were

compared to EpCAM$^+$GFP$^-$ +Ova group. **D,E.** Changes in IEC composition in organoids treated with cytokines (**D**) or co-cultured with polarized Th cells (**E**). Relative abundance (odds-ratio, y-axis) of each IEC-type (by clustering, STAR Methods) under each condition *vs.* their proportions in control organoids (dashed line). * $p < 0.01$, ** $p < 10^{-4}$ (hypergeometric test, error bars: 95% confidence interval for the odds ratio). **F.** IL-10 reduces and IL-13 increases ISC differentiation in organoids. Left and Middle: Diffusion maps for control and IL-10 (top) or IL-13 (bottom) treated organoids. Cells (points) colored by type (left; inset: stem cells) or condition (middle). Right: Distribution of cells (points) along the differentiation pseudotime (STAR Methods). *** $p \ll 10^{-5}$, Mann-Whitney U-test. **G.** Cytokine pre-treatment alters clonogenicity. Relative clonogenicity of organoid cultures (y-axis) of equal organoids number re-seeded post-IL-10 or IL-13 treatment (x-axis). Dots: technical replicates. Error bars: SD, * $p < 0.05$, *** $p < 0.0005$, t-test.
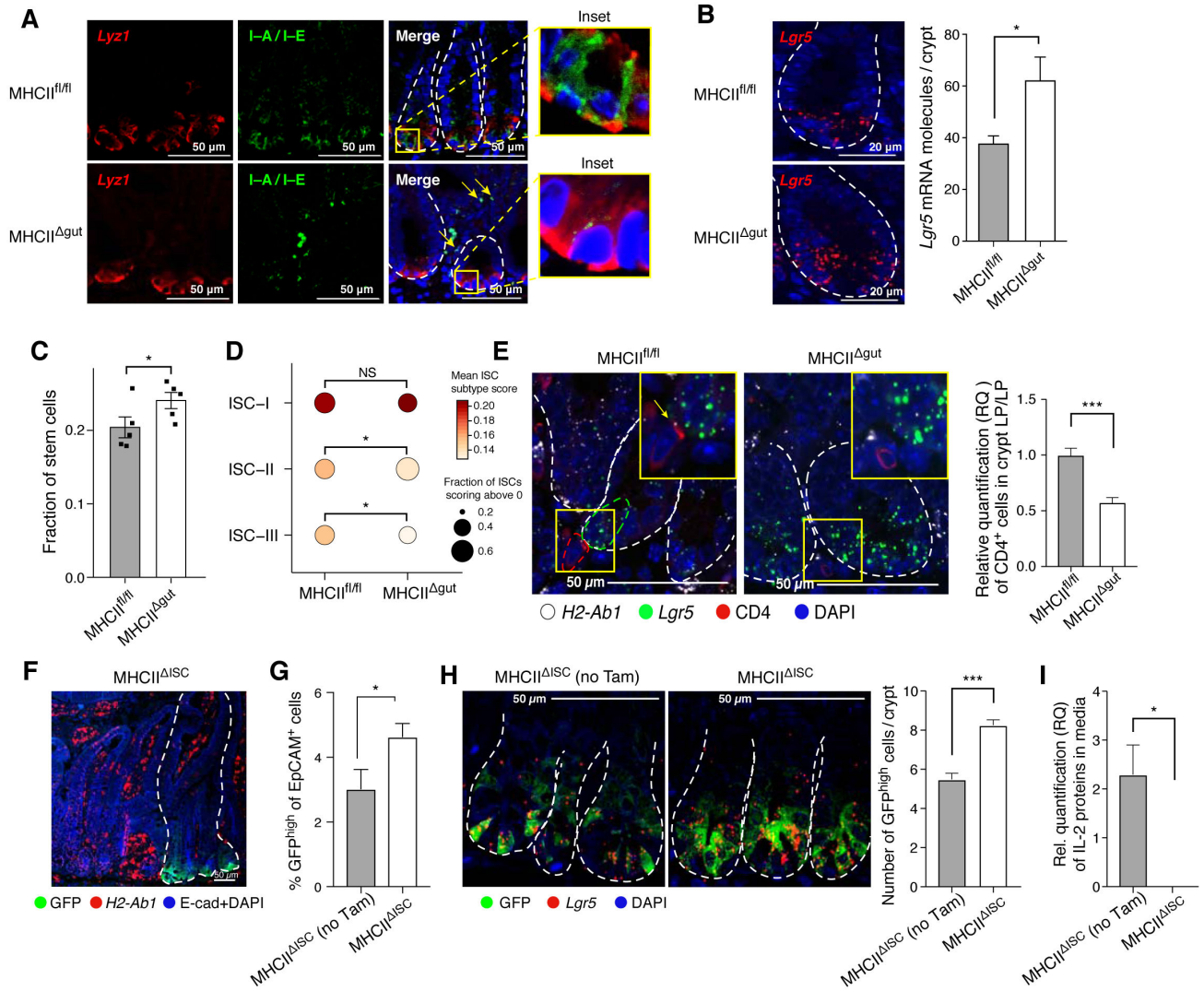
Figure 3. Lgr5$^+$ ISC pool expands following epithelial specific ablation of MHCII.
A. MHCII expression in IECs of MHCII^{gut} mouse. IFA of Lyzl (red) and MHCII (I-A/I-E, green). Inset, x5 magnification. Yellow arrows: MHCII$^+$ cells in LP. Scale bar, 50μm. **B.** Increased Lgr5 expression in crypts of MHCII^{gut} mice. Representative single molecule FISH (smFISH, left) and quantification (right) of *Lgr5* expression (red) within intestinal crypts of MHCII$^{fl/fl}$ and MHCII^{gut} mice. Scale bar, 20μM. *n*=2 mice, 8 fields per mouse. Error bars: SEM (* *p*<0.05, *t*-test). **C.** Increased ISC pool in MHCII^{gut} mice. Fraction of ISCs out of EpCAM$^+$ cells (*y*-axis, from scRNA-seq clustering) in MHCII$^{fl/fl}$ and MHCII^{gut} mice (points, *x*-axis). Error bars: SEM. (* FDR<0.05, likelihood-ratio test). **D.** Decreased ISC-II and -III scores in MHCII^{gut} mice. Fraction of ISCs expressing a signature (circle size) and the signature's mean score in those expressing cells (color bar) for each ISC subset signature (rows) in each genotype (columns). * *p*<0.05, Mann-Whitney U-test. **E.** Th cell number reduction in crypt LP of MHCII^{gut} mice. Combined smFISH and IFA of small intestine from MHCII$^{fl/fl}$ and MHCII^{gut} mice. Left: representative images; yellow arrow: CD4$^+$ cell adjacent to Lgr5$^+$ ISCs; scale bar, 50μm; Inset, x3 magnification. Right: relative

quantification (RQ, *y*-axis) of the number of CD4$^+$ cells per crypt LP/total LP. *n*=3 mice, 8 fields per mouse (*** *p*<0.0001, *t*-test, error bars: SEM). **F.** *H2-Ab1* is deleted in GFP $^+$Lgr5$^+$ ISCs and their progeny. Combined smFISH and IFA in IECs emerging from GFP labeled crypts (dashed line) *vs.* non-labeled crypts. High expression of *H2-Ab1* is found in both the non-labeled crypts and in the LP. Scale bar: 50μm. **G,H.** Increased Lgr5$^+$ ISC fraction in MHCII ^{ISC}. **G.** Bar plot of the percentage (*y*-axis, by FACS, see also Figure S4H) of GFP^{high} cells in MHCII ^{ISC} or matching non-tamoxifen induced controls (MHCII ^{ISC} (no Tam)). *n*=5 mice, * *p*<0.015. **H.** Combined smFISH and IFA of 10 days tamoxifen (MHCII ^{ISC}) and non-tamoxifen (MHCII ^{ISC} (no Tam)) -induced mice. Left: representative images; scale bar, 50μm. Right: Number of Lgr5$^+$ ISCs (GFP^{high}) per crypt (*y*-axis). *n*=3 mice, 8 fields per mouse (*** *p*<0.0001, *t*-test, error bars: SEM). **I.** Lgr5$^+$ ISCs of MHCII ^{ISC} mice do not activate naïve Th cells in co-culture. IL-2 secreted in the media (RQ, *y*-axis) of naïve OTII cells cultured with Lgr5$^+$ ISCs from MHCII ^{ISC} or non-tamoxifen MHCII ^{ISC} controls (no Tam) in presence of 15μg/mL Ova peptide (*n*=3 mice, * *p*<0.05, *t*-test, error bars: SEM). Each group was compared to the EpCAM$^+$GFP$^-$ group (as in Figure 2C).
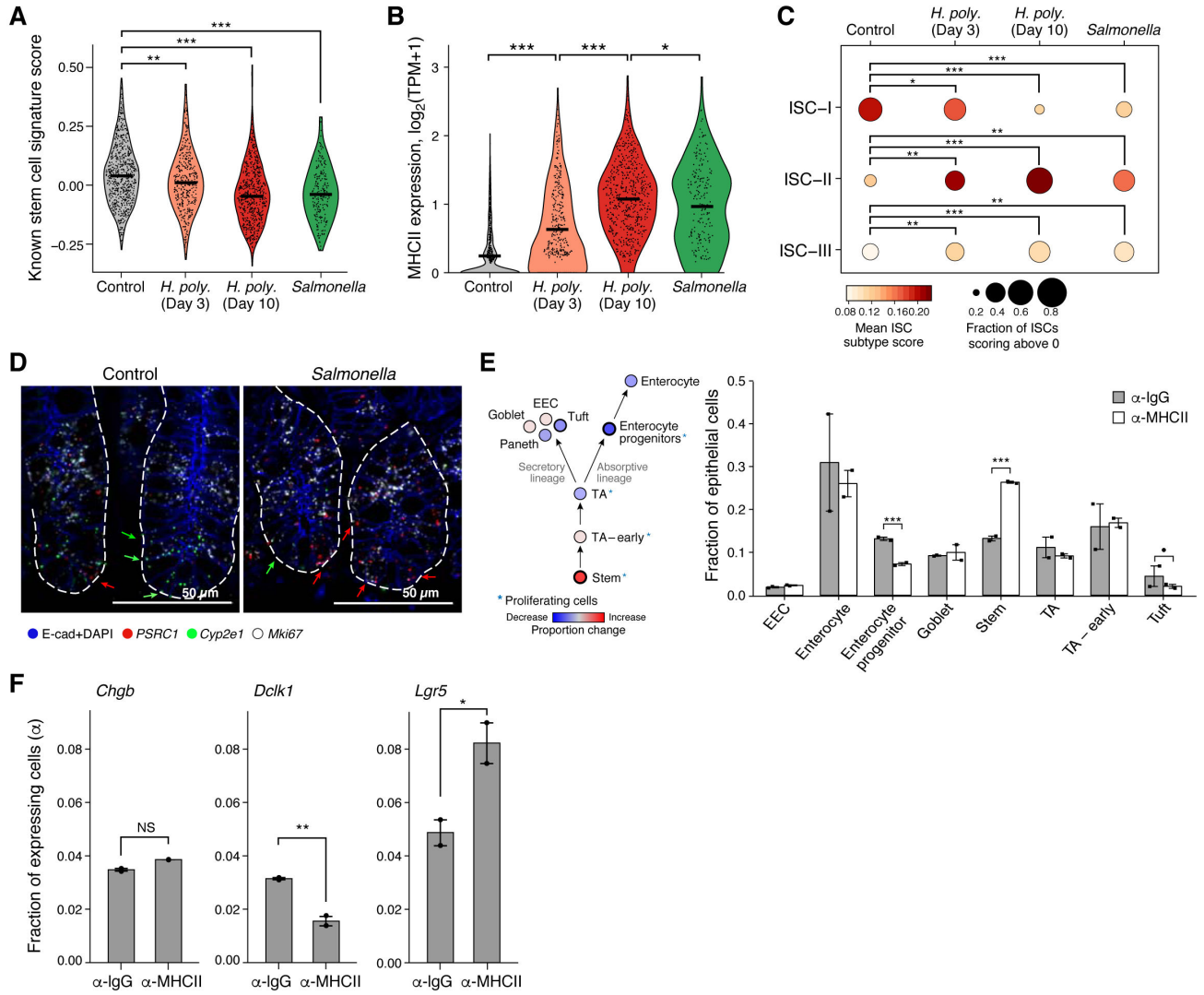
Figure 4. IEC remodeling under pathogenic infection driven by shifts in ISCs.
A,B. Reduced stemness and increased MHCII expression scores in ISCs during pathogenic infection. Distribution of stemness signature (**A**) and MHCII expression (**B**) scores (*y*-axis) in 1,857 ISCs from scRNA-seq (Haber et al., 2017). ** p<0.01, *** p <10^{-5} (Mann-Whitney U-test). **C,D.** Shifts in ISC subsets under infection. **C.** Fraction of ISCs expressing a signature (circle size) and the signature's mean score in those expressing cells (color bar) for each ISC subset signature (rows) in each condition (columns). * p<0.001, ** p<10^{-5}, *** p<10^{-10}, Mann-Whitney U-test. **D**. Combined smFISH and IFA of crypts at homeostasis (left) and two days post-infection (right). Green arrow: Cyp2e1^{+} cell, red arrow: PSRC1^{+} cell; scale bar: 50μm. *Cyp2e1*: ISC-I marker (green), *Psrc1*: ISC-III marker (red). **E.** α-MHCII leads to changes in cell proportions. Right: Frequencies (*y*-axis, unsupervised clustering) of each cell subtype (*x*-axis) in mice infected with *H. polygyrus* and treated with either α-MHCII (white bars) or with α-IgG (grey bars). *** p<10^{-10} (likelihood-ratio test). Left: schematic summary of changes in cell proportions in each cell type (node) (red: increase, blue: decrease; scale bar, bottom). Bold outline: statistically significant; *

proliferating cells. **F**. Reduction in tuft cell and increase in Lgr5^{+} ISC proportions following α-MHCII during *H. polygyrus* infection. Frequency of cells expressing *Chgb, Delh1* or *Lgr5* by scRNA-seq (*y*-axis) 3 days post-infection and treated with either α-IgG or α-MHCII (*x*-axis). * FDR<0.1, ** FDR<0.01 (likelihood-ratio test). Error bars: SEM.
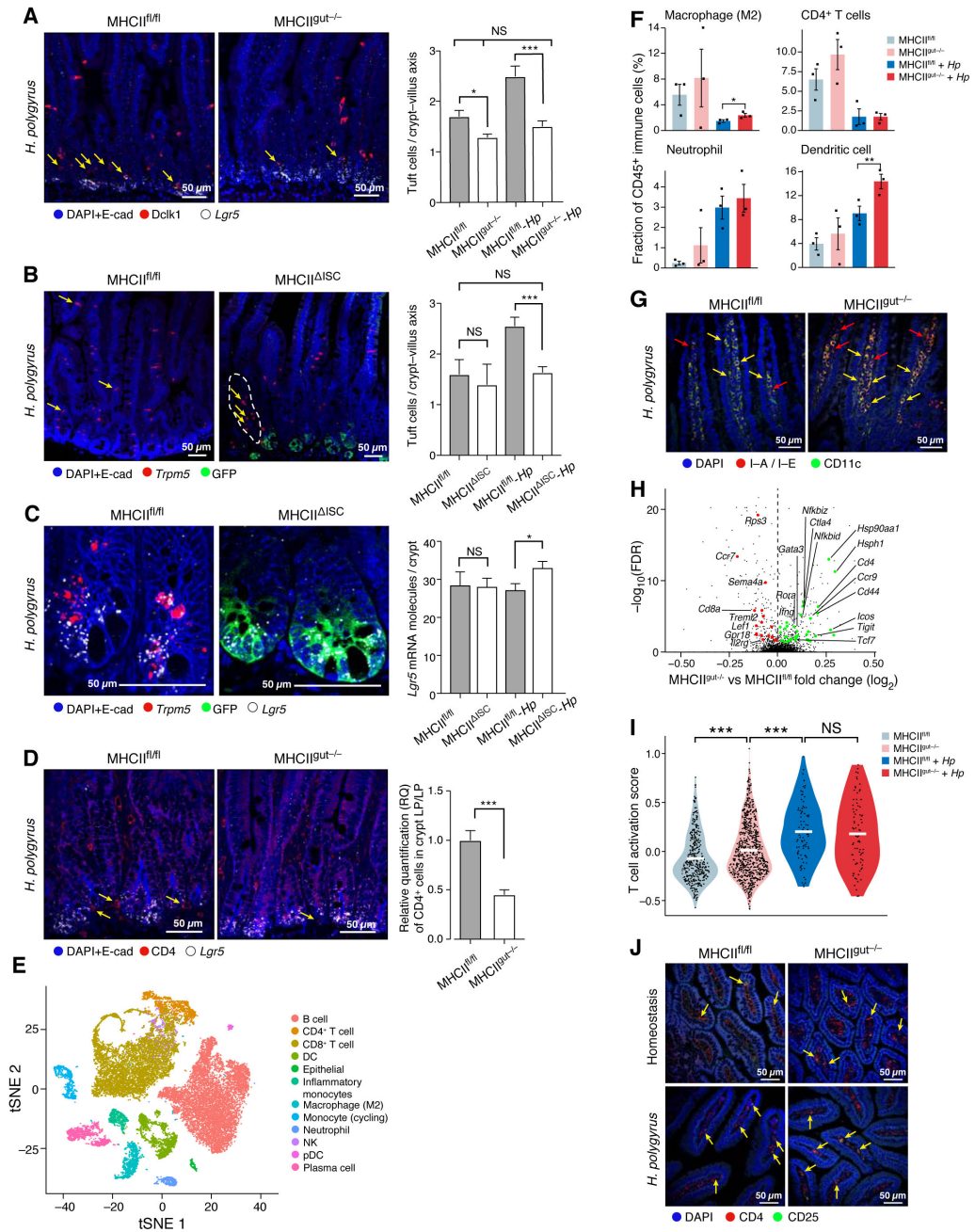
Figure 5. Deletion of epithelial MHCII disrupts mucosal immune responses.

A,B. *H. polygyrus*-induced tuft cell hyperplasia is abolished in IEC-MHCII KO mice. Left: Representative images of combined smFISH and IFA of proximal SI from MHCII^fl/fl and MHCII^gut−/− (**A**) or MHCII^fl/fl and MHCII^ΔISC (**B**) at 4 days (**A**) or 10 days (**B**) post-infection. **A.** Scale bar, 50μm; Yellow arrows: Dclk1^+ cells emerging from the crypt. **B.** scale bar, 50μm. Yellow arrows; mature *Trpm5*^+ villus tuft cells. Dashed line: a crypt in which GFP is absent and ISC^fl/fl reside due to the mosaic knockout in MHCII^ΔISC This crypt-villus axis is associated with higher tuft cell numbers. Right: Number of Dclk1^+ (**A**) or *Trpm5*^+ (**B**) tuft cells per crypt-villus axis (*y*-axis). *n*=3 (**A**) or 4 (**B**) mice per group, 10 fields per mouse

(NS: not significant, * $p<0.05$, *** $p<0.0001$, t-test, error bars: SEM). **C.** *H. polygyrus* infection increases Lgr5 expression in MHCII$^{\sigma ISC}$ mice. Left: Representative images of combined smFISH and IFA of proximal SI from MHCII$^{fl/fl}$ and MHCII ^{ISC} mice 10 days post-infection. Scale bar, 50μm. Right: Number of *Lgr5* mRNA molecules per crypt (y-axis). n=4 mice, 10 fields per mouse (NS: not significant, * $p<0.05$, t-test, error bars: SEM). **D.** Reduced number of crypt Th cells in MHCII$^{gut-/-}$ mice 4 days post-infection. Left: representative images from combined smFISH and IFA of SI from MHCII$^{fl/fl}$ and MHCII$^{gut-/-}$ mice. Scale bar, 50μm. Yellow arrows: CD4$^+$ cells in close proximity to Lgr5$^+$ cells. Right: Relative quantification (RQ) of CD4$^+$ cells per crypt LP/total LP (y-axis). n=3 mice per genotype, 10 fields per mouse (*** $p<0.0001$, t-test, error bars: SEM). **E.** LP immune cell types by scRNA-seq. tSNE of 24,649 CD45$^+$ LP cells at homeostasis and 4 days post-infection (n=12 mice), colored by clustering and annotated *post-hoc* (STAR Methods). **F,G.** Increased APC proportions in MHCII$^{gut-/-}$ mice 4 days post-infection. **F.** Fraction of immune subsets by clustering (from **E**, y-axis) of MHCII$^{fl/fl}$ and MHCII$^{gut-/-}$ mice (points) at homeostasis and 4 days post-infection (x-axis, color code). Error bars: SEM. (* FDR<0.05, ** FDR<0.005, likelihood-ratio test). **G.** Representative IFA images of SI from MHCII$^{fl/fl}$ and MHC$^{gut-/-}$ 4 days post-infection. Scale bar, 50μm; yellow arrows: double positive cells, red arrows: CD11c$^-$MHCII$^+$ cells. **H-J.** Increased Th cell activation in MHC$^{gut-/-}$ at homeostasis. **H.** Mean log$_2$ fold-change (x-axis) and significance ($-\log_{10}$(FDR)) of DE genes between Th cells of MHCII$^{gut-/-}$ mice (765 cells, n=3 mice) and MHCII$^{fl/fl}$ controls (385 cells, n=3 mice) at homeostasis. Green/red dots: up/down-regulated Th cell activation genes (FDR<0.05, likelihood-ratio test). **I.** Distribution of Th cell activation signature scores (y-axis) in 1,319 cells from MHCII$^{gut-/-}$ (846 cells, n=3 mice) and MHCII$^{fl/fl}$ controls (473 cells, n=3 mice) at homeostasis and 4 days post-infection (color legend). White bars: mean. *** $p<10^{-5}$, NS: not significant, Mann-Whitney U-test. **J.** Representative images of IFA of SI villi of MHCII$^{fl/fl}$ and MHCII$^{gut-/-}$ mice at homeostasis (top) and 4 days post-infection (bottom). Scale bar, 50μm, arrow: CD25$^+$ CD4$^+$ cell.
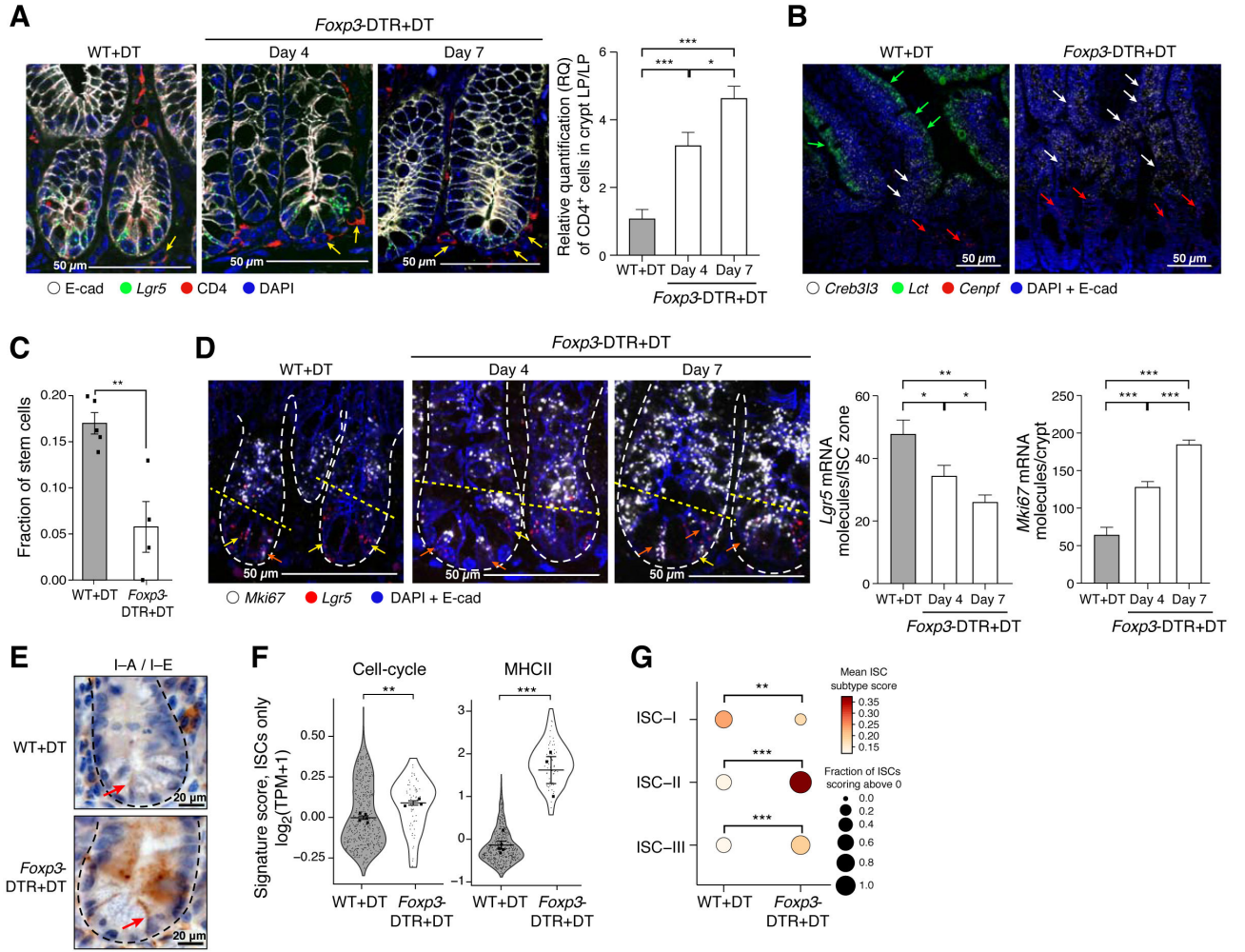
Figure 6. T_reg ablation decreases the Lgr5+ ISC pool.
A. Increase in CD4+ cells in T_reg ablated crypts. Combined smFISH and IFA of SI from wild-type (WT) or *Foxp3*-DTR mice treated with diphtheria toxin (DT) for 4 or 7 days. Left: representative images. Arrows: CD4+ cells adjacent to Lgr5+ ISCs; scale bar, 50μm. Right: Relative quantification (RQ) of CD4+ cells per crypt LP/total LP (*y*-axis). *n*=2 mice, 8 fields per mouse per time point (**p*<0.02, ** *p*<0.0003, *t*-test, error bars: SEM). **B.** Depletion of mature enterocytes post-T_regs ablation. Combined IFA and smFISH of SI in WT and *Foxp3*-DTR mice treated with DT. *Lct*: mature enterocyte marker, *Creb3l3* and *Cenpf*: early enterocyte markers (Haber et al., 2017). Green, red, white arrows: *Lct*+, *Cenpf*+, and *Creb313*+ cells, respectively. Scale bar, 50μm. **C.** Reduction in ISC numbers following T_reg ablation. Fraction of ISCs among EpCAM+ cells (*y*-axis, by clustering) in WT and *Foxp3*-DTR mice 7 days post-DT treatment. Error bars: SEM. (** FDR<0.005, likelihood-ratio test, STAR Methods). **D.** Reduced Lgr5 expression and increased cell proliferation following T_reg ablation. Combined smFISH and IFA of SI from WT and *Foxp3*-DTR mice treated with DT for 4 or 7 days. Left: representative images. Yellow arrows: *Mki67*-Lgr5+ ISCs, orange arrows: *Mki67*+Lgr5+ ISCs, scale bar, 50μm. Right: Number of *Lgr5* (mid-right) and *Mki67* (right) molecules per crypt (*y*-axes). *n*=2 mice, 8 fields per mouse per time point (**p*<0.05,

** $p<0.001$, *** p$<$ 0.0001 t-test, error bars: SEM). **E-F.** Increased MHCII expression in ISCs of T$_{reg}$-depleted mice. **E.** IHC of MHCII (I-A/I-E; brown) co-stained with hematoxylin (blue) within the intestinal crypt of WT and *Foxp3*-DTR mice treated for 7 days with DT. Arrows: MHCII$^+$Lgr5$^+$ ISC. **F.** Distribution of the scores for cell cycle (left) and MHCII (right) genes in ISCs from WT (n=5; 464 cells) and *Foxp3*-DTR (n=4; 62 cells) mice 7 days post-DT. Squares: mean score per mouse; thick bar: overall mean; error bars: SEM. (* $p<0.05$, ** $p<0.005$, *** $p<5\times10^{-4}$, likelihood-ratio test). **G.** Changes in ISC subsets in T$_{reg}$-depleted mice. Fraction of ISCs expressing a signature (circle size) and the signature's mean score in those expressing cells (color bar) for each ISC subset signature (rows) in each genotype (columns). ** $p<10^{-5}$, *** $p<10^{-10}$, Mann-Whitney U-test.
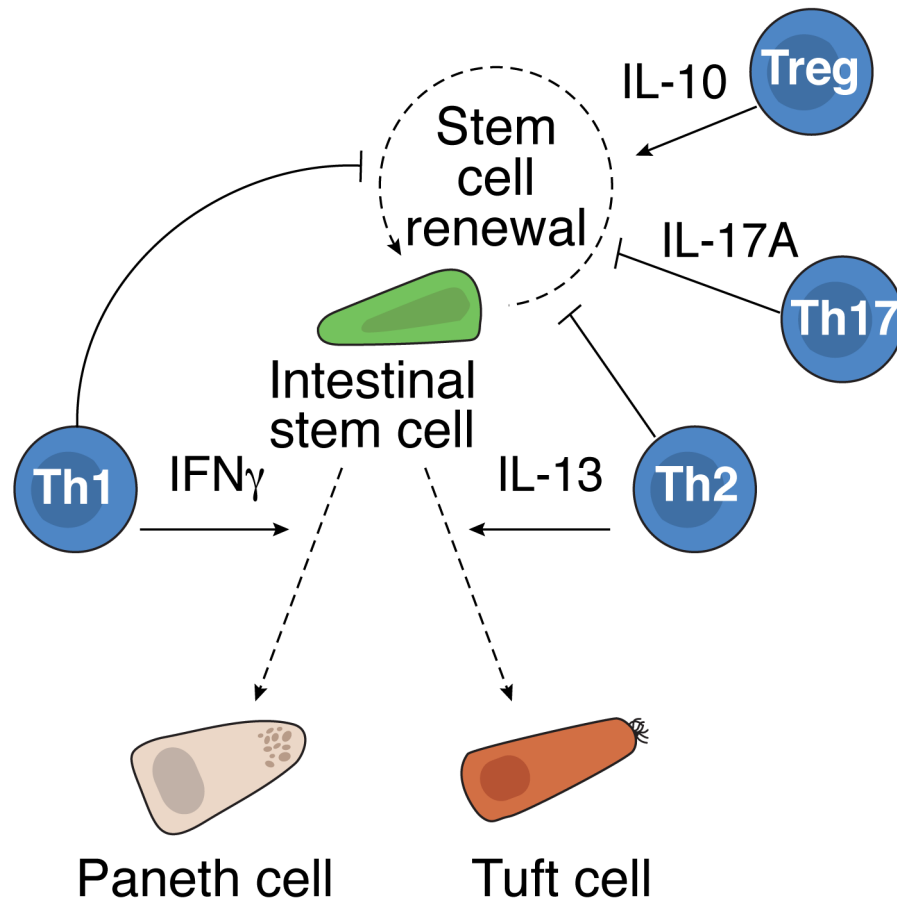
Figure 7. A model of the cross-talk between Th cells and ISCs.
Th subsets (blue nodes) modulate (solid arrows) the fate (dashed arrows) of Lgr5$^+$ ISCs (green). T$_{regs}$ and their key cytokine IL-10 promote stem cell renewal, while Th17 cells and their cytokine IL-17a reduce stem cell renewal and promote differentiation. Both Th1 and Th2 (and their cytokines) suppress stem cell renewal and promote specific differentiation towards Paneth cells (tan) and tuft cells (orange), respectively.